

JGR Space Physics

RESEARCH ARTICLE

10.1029/2019JA027307

Key Points:

- The high-frequency breakpoint in the solar wind's magnetic power spectral density and the power above the breakpoint are of interest
- The power spectrum of individual solar wind current sheets has the same shape as the power spectrum of the solar wind above the breakpoint
- The density of current sheets in the solar wind is sufficient to account for the spectral power of the solar wind above the breakpoint

Correspondence to:

J. E. Borovsky, jborovsky@spacescience.org

Citation:

Borovsky, J. E., & Burkholder, B. L. (2020). On the Fourier contribution of strong current sheets to the high-frequency magnetic power spectral density of the solar wind. *Journal of Geophysical Research: Space Physics, 125*, e2019JA027307. https://doi.org/10.1029/2019JA027307

Received 15 AUG 2019 Accepted 17 DEC 2019 Accepted article online 17 JAN 2020

On the Fourier Contribution of Strong Current Sheets to the High-Frequency Magnetic Power Spectral Density of the Solar Wind

Joseph E. Borovsky¹ and Brandon L. Burkholder²

¹Space Science Institute, Boulder, CO, USA, ²Embry-Riddle Aeronautical University, Daytona Beach, FL, USA

Abstract The hypothesis is explored that the high-frequency magnetic spectral power of the solar wind is associated with the spatial profiles of strong current sheets (directional discontinuities) in the solar wind plasma. This hypothesis is based on previous findings about current sheets and the solar wind's magnetic power spectra (1) that the amplitude distribution and waiting time distribution of strong current sheets determines the amplituic composition and the electron strade and spectral slope of the "inertial range" of frequencies and (2) that the thicknesses of strong current sheets in the solar wind determine the breakpoint frequency that ends the inertial range. Solar wind current sheets are collected from the WIND 0.09375-s and MMS 7.8×10^{-3} -s magnetic data sets, and the current sheets are individually Fourier transformed. At frequencies above the solar wind breakpoint (1) the shape of the magnetic power spectra of the current sheets resembles the shape of the magnetic power spectra of the solar wind and (2) the current sheets occur frequently enough to account for the magnetic power of the solar wind above the breakpoint. This has implications for the physics underlying the high-frequency magnetic power spectral density of the solar wind, supplementing the energy-cascade description of the high-frequency spectrum.

1. Introduction

The magnetic power spectral density (PSD) of the solar wind (the square of the temporal Fourier transform of the magnetic field time series measured by a spacecraft) is sketched in Figure 1, plotting the magnetic Fourier energy as a function of the frequency in a spacecraft frame (see also Figure 2 of Podesta, 2010a, or Figure 2 of Sahraoui et al., 2010). The power spectrum seen is attributed to spatial structures in the solar wind magnetic field that are advected past the measuring spacecraft. Hence, the spectra are usually converted from frequency f to wave number k, but we will concentrate on frequency in this study. Five features of the spectrum that are pertinent to the present study are labeled in Figure 1. The first is the "inertial range" at lower frequencies in this sketch. The inertial range of frequencies corresponds to spatial scales in the solar wind that are in the MHD range of scale sizes, from somewhat larger than gyroradii and inertial lengths up to a few percent of an AU. On the spacecraft, the time scales are seconds to hours. The inertial range is characterized by a power law $f^{-\alpha}$ where α is often in the range 1.5–1.7 (Borovsky, 2012a; Coleman, 1968; Podesta et al., 2007; Siscoe et al., 1968). The second feature is the "breakpoint" in the magnetic power spectrum at the high-frequency end of the inertial range where the power spectrum steepens. The breakpoint frequency corresponds to solar $wind \ scale \ sizes \ in \ the \ vicinity \ of \ ion \ gyroradii \ and$ ion inertial lengths. The third region is denoted here as the "high-frequency-1 range," also known as the "dissipation range" or "dispersion range." The magnetic power spectrum above the breakpoint is often fit by a power law $f^{-\beta}$ with a range of β values found in the literature: Examples are $\beta \sim 2-4.5$ (Leamon et al., 1998), $\beta \sim 1-4$ (Smith et al., 2006), $\beta \sim 2.8$ (Alexandrova et al., 2009), $\beta \sim 3.81$ (Podesta, 2010a), $\beta \sim 3.96$ (Sahraoui et al., 2010), β ~ 2.8-3.0 (Chen et al., 2014), and β ~ 2.7 (Bruno et al., 2017). The high-frequency spectrum above the breakpoint is usually attributed to kinetic plasma waves and their interactions and damping. A second breakpoint appears at a frequency higher than the breakpoint ending the inertial range. At "breakpoint-2" the steep spectrum in high-frequency-range-1 becomes shallower in high-frequency-range-2 (Podesta, 2010a; Sahraoui et al., 2010).

Strong current sheets account for much of the Fourier power of the solar wind (Borovsky, 2010; Li et al., 2011, 2012; Siscoe et al., 1968). By creating an artificial time series that contains the information about the magnetic field changes across strong solar wind current sheets and none of the information about the

©2020. American Geophysical Union. All Rights Reserved.



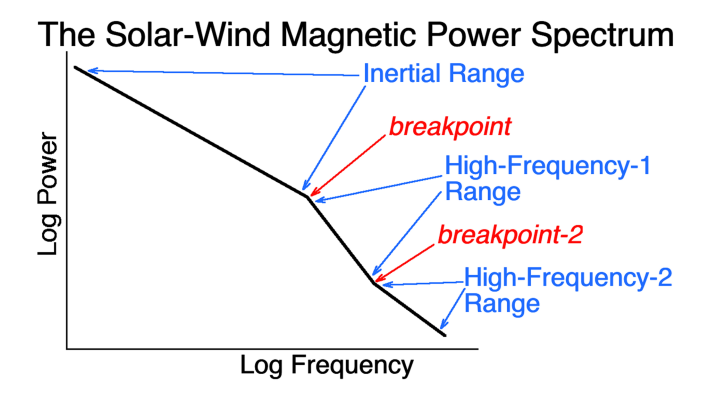


Figure 1. A sketch of the magnetic power spectral density of the solar wind with the features that are germane to this study labeled.

solar wind magnetic fluctuations between the current sheets, it was found that the PSD of the current sheet time series reproduces the amplitude and spectral slope of the inertial range of the PSD of the actual solar wind time series (Borovsky, 2010). The interpretation is that the distribution of amplitudes of the current sheets (size of the magnetic field jumps across the current sheets) and the distribution of waiting times between subsequent current sheets govern the slope of the inertial range magnetic spectrum.

The thicknesses of the strong current sheets in the solar wind govern the frequency location at which the breakpoint in the solar wind magnetic power spectrum occurs (Borovsky & Podesta, 2015; Podesta & Borovsky, 2016). This has been demonstrated by going into the solar wind magnetic field time series and temporally stretching the time series only within the strong current sheets, which has the effect of thickening the current sheets

but not altering other features in the time series. When the strong current sheets are thickened by a factor X, the magnetic power spectrum breakpoint frequency f_{break} shifts to lower frequencies by a factor of 1/X (Borovsky & Podesta, 2015).

Related to the two effects of strong current sheets described in the previous two paragraphs, it is hypothesized here that the spatial profiles of the current sheets may govern the high-frequency spectral power and spectral slope above the breakpoint. In the present study this hypothesis will be explored via Fourier time series analysis of solar wind current sheets compared with the magnetic power spectra of the full solar wind time series. Magnetic field measurements from WIND with a time resolution of 0.09375 s and from MMS with a time resolution of 7.8×10^{-3} s will be utilized.

This manuscript is organized as follows. In section 2 the data sets and Fourier techniques that are used are described. Section 3 examines the Fourier properties of some artificial current sheets and the dependence of the frequency spectra on the profiles of current sheets. In section 4 the Fourier spectra of solar wind current sheets are examined, and in section 5 the Fourier power of solar wind current sheets is examined. Section 6 contains discussions about the implications for the physics of the solar wind's magnetic spectra and about future studies.

2. Data and Fourier Techniques

Solar wind magnetic field measurements with 0.09375-s time resolution from the WIND MFI instrument (Lepping et al., 1995) and with 7.8×10^{-3} -s time resolution from the Level-2 MMS magnetometer measurements (Russell et al., 2016) are analyzed. Data from the WIND spacecraft are used from 3 January 2005 when the WIND spacecraft was at L1 in the undisturbed solar wind. Data from MMS1 were used from several burst-mode intervals in January 2017 to April 2018 when MMS was in the solar wind.

We are interested in particular in the Fourier signatures of strong current sheets in the magnetic structure of the solar wind, where strong means that the solar wind magnetic field undergoes a significant change in direction in crossing the current sheet and/or there is a significant change in the magnetic field strength across the current sheet.

A collection of 85 current sheets from WIND is made by looking for clear sudden (seconds) rotations of the magnetic field direction. Current sheets that are temporally isolated from other current sheets are taken, with current sheets found near data gaps rejected. A collection of 178 current sheets from MMS is obtained by using temporally isolated current sheets in the Burkholder and Otto (2019) collection of current sheets. Burkholder and Otto selected their current sheets from the MMS mission events list database https://lasp. colorado.edu/mms/sdc/public/about/events/#/ to compile a list of burst-mode intervals labeled as containing a "solar wind current sheet," which ranged from ~30 s to ~3 min. The search algorithm described in Burkholder and Otto (2019) was then applied to select current sheets with sufficient changes in the magnetic field such that they were isolated from periodic fluctuations and other large-scale structure. For the 178 MMS current sheets, the available data are extended to fill the Fourier data subinterval, which is 8.192



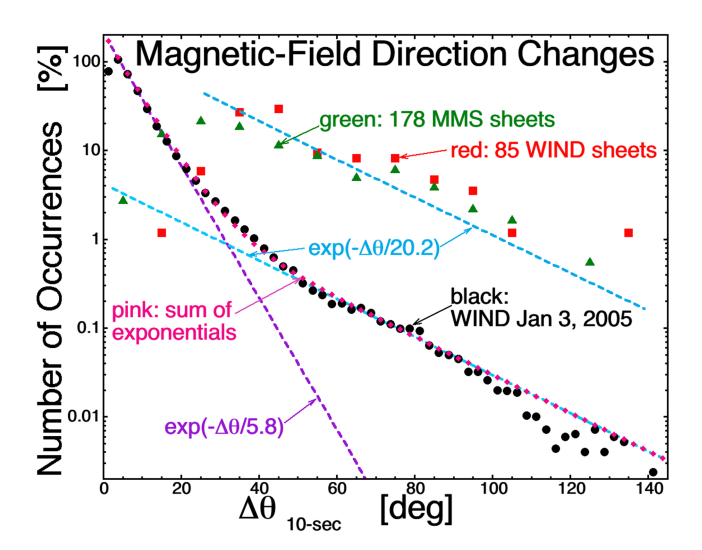


Figure 2. Distributions of the 10-s change in the direction of the solar wind magnetic field vector are plotted. The distribution for the day 3 January 2005 as measured by WIND is plotted as the black round points. The distribution of changes across the 85 WIND current sheets is plotted as the red square points. The distribution of changes across the 178 MMS current sheets is plotted as the green triangles.

data points (64 s) long. To fill the window, the first and last available data values were extended to the beginning and end of the data interval, respectively.

In Figure 2 the distributions of amplitudes of the current sheets are plotted. The 10-s angular change $\Delta\theta$ in the direction of the solar wind magnetic field across the current sheet is measured (comparing the field vector 5 s before the center of the sheet with the field vector 5 s after), and the $\Delta\theta$ values are binned. The distribution of red square points in Figure 2 is the distribution for the 85 WIND current sheets, and the distribution of green triangle points is the distribution of the 178 MMS current sheets. Note that there are a few points in Figure 2 representing current sheets with small 10-s values of $\Delta\theta$: Inspection of these sheets finds that they are either (a) characterized by a strong change in the magnitude B_{mag} of the magnetic field or (b) that the rapid (~1-s) strong rotation of the direction of B is accompanied by a slow rotation back. Plotted as the black circles in Figure 2 are the distribution of 10-s changes in the WIND data set for the entire day 3 January 2005. (This distribution is multiplied by a factor of 4.) The 3 January distribution exhibits a double-exponential shape (see also Figure 2 of Borovsky, 2008, Figure 6 of Miao et al., 2011, or Figure 3 of Borovsky, 2020a). At low values of $\Delta\theta$ the black points are fit with an exponential of the form $\exp(-\Delta\theta/5.8^{\circ})$; purple dashed curve), and at high $\Delta\theta$ values the black points are fit with an exponential of the

form $\exp(-\Delta\theta/20.2^\circ;$ lower light blue dashed curve). The sum of the two exponential fits is plotted as the pink diamond-shaped points: As can be seen, the black points are well fit by the sum of two exponentials. Following Borovsky (2008), the $\exp(-\Delta\theta/20.2^\circ)$ distribution is taken to be the distribution of $\Delta\theta$ values across current sheets in the solar wind and the $\exp(-\Delta\theta/5.8^\circ)$ distribution is taken to be the distribution of $\Delta\theta$ values in the magnetic field fluctuations between the current sheets. Copying the light blue $\exp(-\Delta\theta/20.2^\circ)$ fit and moving it upward on the plot into the red and green points, it is seen that the shapes of the distributions of $\Delta\theta$ values in the collection of 85 WIND current sheets and in the collection of 178 MMS current sheets are typical for current sheets in the solar wind.

PSDs are constructed from the magnetic field time series using the FFT (fast Fourier transform) periodogram method (cf. Otnes & Enochson, 1972). Windowing is used to isolate the time signal of each current sheet in each data subinterval. To avoid leakage into the high-frequency portions of the PSD, Gaussian-based windows are used (cf. Figure 1 of Borovsky & Podesta, 2015). The three window types used are shown in Figure 3. The windows are the Gaussian

$$W_{G}(t) = \exp\left(-\left[(t-t_{o})/t_{gauss}\right]^{2}\right) \tag{1}$$

where t_o is the center of the Gaussian (i.e., the location of the current sheet in the data subinterval), the exponential-4 window

$$W_4(t) = \exp\left(-\left[(t - t_o)/t_{gauss}\right]^4\right) \tag{2}$$

and the exponential-8 window (cf. Appendix B of Borovsky, 2012a)

$$W_8(t) = \exp\left(-\left[(t - t_o)/t_{gauss}\right]^8\right). \tag{3}$$

In all three windows, t_{guass} is the halfwidth of the window. The Fourier signal of the Gaussian window exp $(-](t-t_o)/t_{gauss}]^2$) is a Gaussian in the PSD $\exp(-f^2/f_{gauss}^2)$, with $f_{gauss}=1/(2^{1/2}\pi t_{gauss})$. If the Gaussian window has a half width $t_{gauss}=9.375$ s, then $f_{gauss}=2.40\times 10^{-2}$ Hz and the Gaussian filter will not contribute to the PSD for frequencies higher than a few times f_{gauss} . The exponential-4 and exponential-8 windows have similar properties.



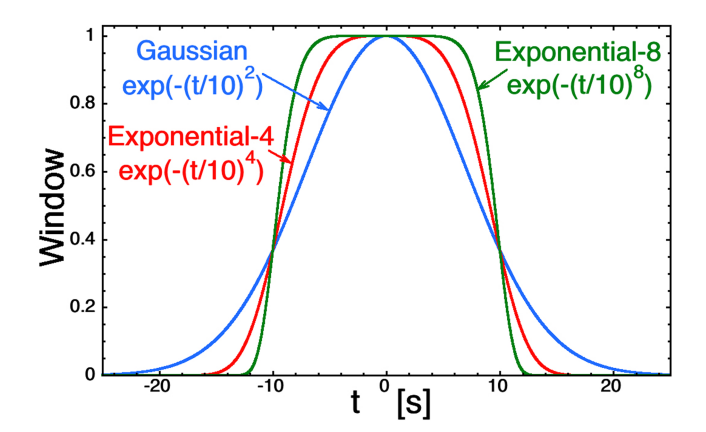


Figure 3. The three windows to isolate current sheets in the solar wind data are plotted here with halfwidths of 10 s.

Two examples of windowed current sheets are shown in Figure 4. In Figure 4a an unwindowed WIND magnetic field time series $B_x(t)$, $B_y(t)$, and $B_z(t)$ (GSE coordinates) are shown. Note the large amplitude of the current sheet as seen in B_y . Figure 4b shows the time series after applying the Gaussian window with $t_{gauss} = 9.375$ s (which is 100 data points in the WIND MFI data). In B_y one can see the Gaussian pulse with a current sheet in it. Figure 4c shows the WIND data windowed by the exponential-8 window with $t_{gauss} = 0.09375$ s. Figure 4d shows an unwindowed current sheet interval in the MMS data. Note the extensions of the data interval before t = -14.1 s and after t = 13.9 s. Figures 4e and 4f show the Gaussian windowed data and the exponential-8 windowed data, both with halfwidths $t_{gauss} = 9.375$ s, which is 1,200 MMS data points.

Spectral slopes are calculated from the magnetic PSDs using linear regression fits of log10(power) as a function of log10(frequency). The standard method is utilized in which all available PSD data points are used for

the least squares fit. This differs from the least squares fit method suggested by Podesta (2016) wherein the available periodogram data are interpolated onto a uniformly spaced grid in log (frequency) and the grid points are then used for the least squares fit. The standard method favors the higher-frequency portion of the frequency range since that portion contains a higher density of data points (Podesta, 2016).

3. Mathematically Generated Current Sheets

To demonstrate the effect of the profiles of current sheets on the magnetic PSD, Figure 5a plots six mathematically generated artificial current sheets B(t) as functions of time. The blue curve with points is a linear ramp. Note that a linear ramp has continuous zeroth derivatives B(t) and discontinuous first derivatives dB/dt. The dark blue curve without points is the cube of the linear ramp $(B(t))^3$: The "linear³ ramp" also has continuous zeroth derivatives and discontinuous first derivatives. The red curve with points in Figure 5a is a ramp constructed from a half sine wave. This "half-sine ramp" has continuous zeroth and first derivatives but discontinuous second derivatives d^2B/dt^2 . The orange curve without points is the cube of the half-sine ramp $(B(t))^3$: This "half-sine³ ramp" also has continuous zeroth and first derivatives but discontinuous second derivatives. The dark green curve with points in Figure 5a is a hyperbolic tangent ramp. The tanh ramp has an infinite number of continuous derivatives. The light green curve without points is the cube of the tanh ramp $(B(t))^3$: The "tanh³ ramp" also has an infinite number of continuous derivatives.

In Figures 5b–5d the PSDs of the six ramps of Figure 5a are plotted. Prior to constructing the PSDs, the ramps B(t) were windowed with a Gaussian window with a fullwidth of 45 s. Figure 5b shows the PSDs of the linear ramp and the linear³ ramp. The Fourier spectral slope associated with a linear ramp (blue) can be seen in Figure 5b to be f^{-4} (see also Figure 1 of Borovsky & Podesta, 2015). Note that the PSD of the linear³ ramp (dark blue) is similar to the PSD of the linear ramp even though the linear³ ramp in Figure 5a has a complicated inflection at time t=0. The Fourier power of the linear³ ramp is slightly larger than that of the linear ramp, but the spectral slope is still f^{-4} owing to the discontinuous first derivatives.

In Figure 5c the spectral slope of the half-sine ramp (red) with discontinuous second derivatives can be seen to be f^{-6} , and the half-sine³ (orange) also with discontinuous second derivatives has a spectral slope that is also f^{-6} , but with slightly more spectral power at high frequencies.

The hyperbolic tangent ramp (dark green) and the tanh³ ramp (light green) in Figure 5d have spectra that cannot be fitted by a power law since they have infinite continuous derivatives. Again, the tanh³ spectrum has more high-frequency power than does the tanh spectrum.

4. The Fourier Spectra of Solar Wind Current Sheets

The blue curve in Figure 6 is the average of the magnetic PSDs of the 85 individual current sheets in the WIND MFI data set. Prior to Fourier transforming, the time series subinterval containing each current sheet was windowed with a Gaussian with a halfwidth of 9.375 s. The PSD of the 9.375-s Gaussian window itself is plotted in purple in Figure 6. Plotted in green in Figure 6 is a solar wind PSD: A data interval 3.41-hr long was

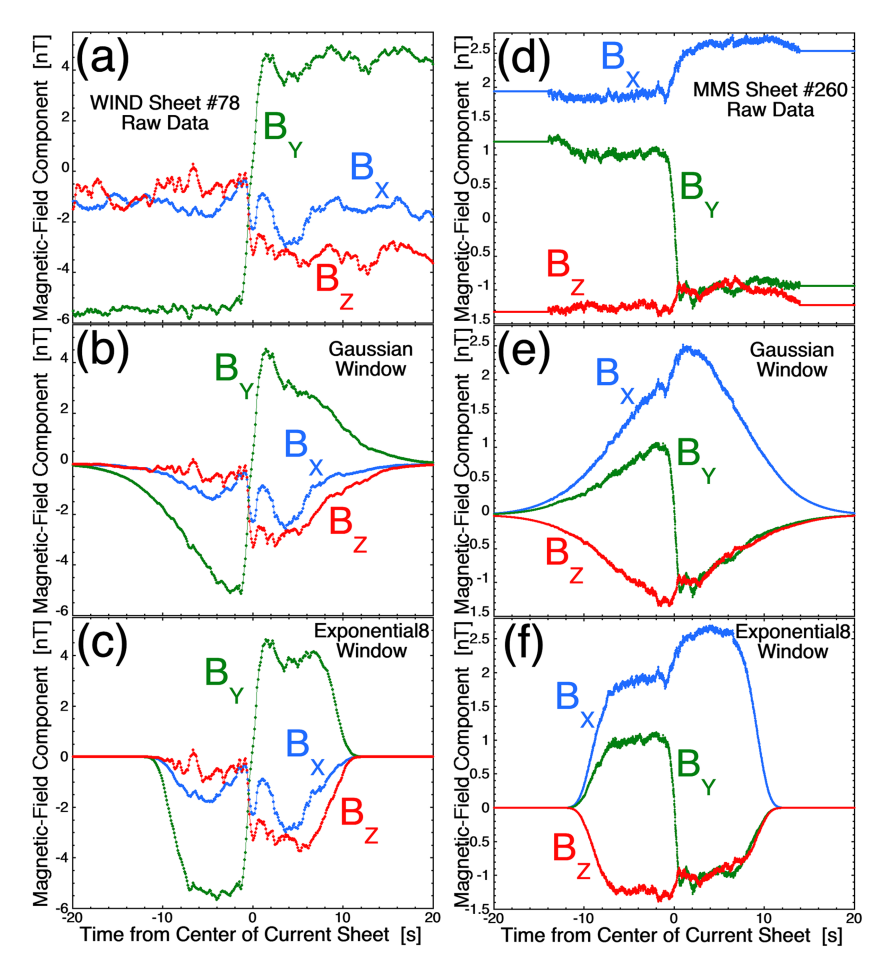


Figure 4. The component magnetic field (GSE coordinates) for two current sheets are shown. In panels (a) and (d) the current sheets are shown unwindowed, with a WIND current sheet in panel (a) and an MMS current sheet in panel (b). In panels (b) and (e) the WIND and MMS current sheets (respectively) are shown after applying a Gaussian window with halfwidth of 9.375 s. In panels (b) and (e) the WIND and MMS current sheets (respectively) are shown after applying an exponential-8 window with halfwidth of 9.375 s.

extracted from the WIND MFI data set at the center of the day 3 January 2005 and that data interval was windowed with a Gaussian with a fullwidth of 51.4 min prior to Fourier transforming. The thin green curve shown only at low frequencies is the PSD of that solar wind interval, and the thicker green curve is a 300-point running average of that solar wind PSD. The breakpoint between the "inertial range" and the "high-frequency spectra" is seen below 0.5 Hz in the green curve.

The Nyquist frequency for the 0.09375-s WIND MFI data is $f_{Nyquist} = 5.33$ Hz and 0.25 $f_{Nyquist} = 1.33$ Hz. Staying away from the Nyquist frequency by a factor of 4 (e.g., Borovsky, 2012a), the valid frequency range of the spectra above the breakpoint is 0.5 Hz \leq $f \leq$ 1.33 Hz for WIND MFI. The spectral slope of the solar wind interval (green curve in Figure 6), obtained with a linear regression fit in log-log space, in the frequency range 0.5–1.33 Hz is -3.21. The spectral slope of the average of the 85 single-sheet PSDs (blue curve) in the frequency range 0.5–1.33 Hz is -3.36. This spectral index is listed in Table 1. The red curve in Figure 6 is formed by (1) producing a Gaussian-windowed data interval for each of the 85 WIND current sheets, (2) assembling the 85 data intervals sequentially into one long data interval, and then (3) Fourier analyzing the long interval containing the sequence of 85 windowed current sheets. Each of the 85 subintervals of this long data interval is 1,024 points long, which introduces a 1024×0.09375 s = 96-s periodicity, or a 1.04×10^{-2} Hz frequency. The thin red curve shown only at lower frequency is the PSD of the train of 85 current sheets, and the thick red curve is a 100-point running average of the PSD. In the frequency range 0.5 Hz \leq $f \leq 1.33$ Hz the spectral slope of the red curve is -3.42.



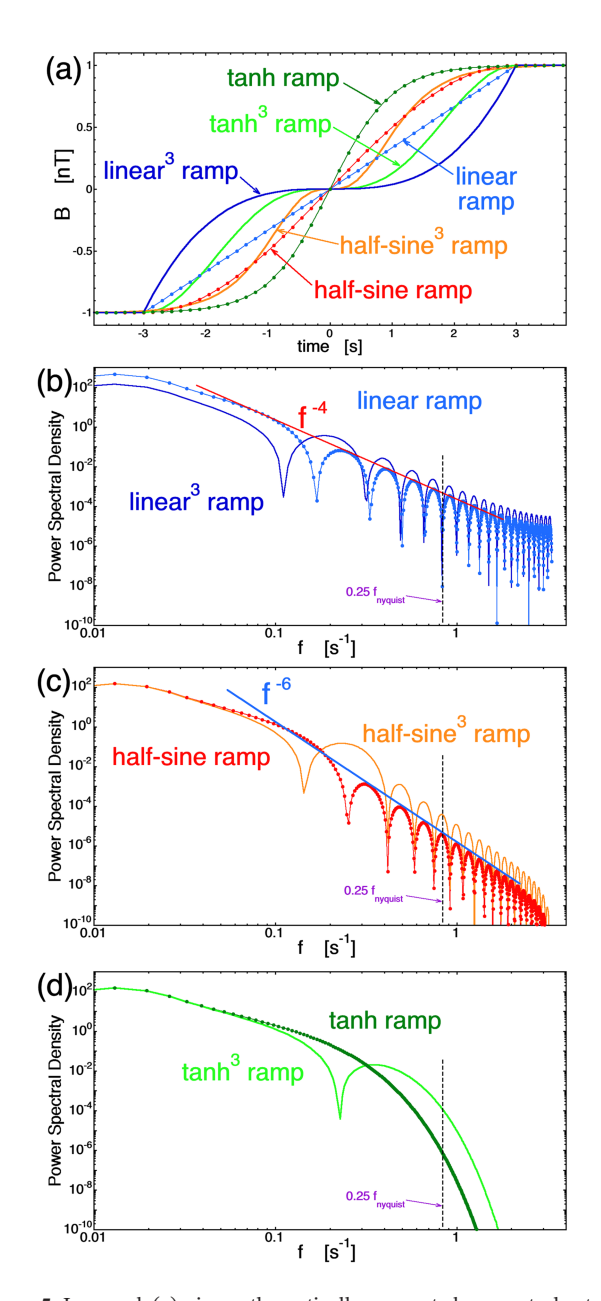


Figure 5. In panel (a) six mathematically generated current sheets are plotted versus time. The six ramps are windowed with a Gaussian (10-s halfwidth), and then their power spectral densities are calculated and plotted in panels (b), (c), and (d) as labeled.

In Figure 7 the occurrence distribution of the individual spectral slopes of the 85 WIND current sheets windowed with 9.375-s halfwidth Gaussians is plotted as the blue solid curve. The distribution of the 85 spectral slopes using exponential-4 and exponential-8 windows is plotted as the solid red and solid green curves, respectively. The mean values of the 85 spectral slopes for the 0.5–1.33 Hz frequency range are –3.64 for the Gaussian window, –3.63 for the exponential-4 window, and –3.62 for the exponential-8 window (cf. Table 1). Interpretation of the distribution of spectral slopes made from finite length data intervals (with the resulting "spectral variance") has been analyzed in Appendix A of Borovsky (2012a): A distribution of measured spectral indices is expected if the data intervals are finite and the mean value of the distribution is the correct value to use for the spectral slope.

For comparison, 311 intervals wherein no strong current sheet resides were located in the WIND MFI 3 January 2005 data set. (Those locations were identified by visual inspection of the plots of the 10-s change in the magnetic field direction, requiring $\Delta\theta_{10\text{-s}}$ to be approximately less than 10° for about 1 min.) The spectral indices in the 0.5 Hz \leq f \leq 1.33 Hz intervals are statistically shallower for the no-sheet intervals than they are for the current sheet intervals: The mean values of the 311 spectral slopes for the are -2.98 for the Gaussian window, -2.98 for the exponential-4 window, and -2.99 for the exponential-8 window. As will be shown in section 5, the Fourier power of the no-sheet intervals is much less than the Fourier power of intervals with a current sheet.

In Figure 8 the average of the 85 WIND current sheet PSDs is plotted for the three types of windows: Gaussian in blue, exponential-4 in red, and exponential-8 in green. The three averaged PSDs are very similar. In the frequency range 0.5-1.33 Hz the spectral slopes are -3.64 for Gaussian, -3.63 for exponential-4, and -3.62 for exponential-8 (cf. Table 1).

Also plotted in Figure 8 are the averages of the 178 individual PSDs for the 178 MMS current sheets windowed with a Gaussian (blue), an exponential-4 (red), and an exponential-8 (green). The Nyquist frequency for the MMS magnetic field data is $f_{\rm Nyquist}=64~\rm Hz$ so $0.25f_{\rm Nyquist}=16~\rm Hz$. Staying away from the Nyquist frequency by a factor of 4, the valid frequency range above the solar wind breakpoint is $0.5~\rm Hz \le f \le 16~\rm Hz$. Note that in this frequency range the spectral slopes in the Figure 8 are steeper in the lower frequency end of the range and become shallower at the higher-frequency end. For comparison with the WIND current sheets and the WIND spectra of the full solar wind, fits to the MMS spectra are made in the range $0.5~\rm Hz \le f \le 1.33~\rm Hz$. In this frequency range the spectral slopes of the averages of the MMS current sheet PSDs are $-2.83~\rm for$

Gaussian windows, -2.75 for exponential-4 windows, and -2.71 for exponential-8 windows (cf. Table 1). These MMS current sheet spectral slopes are shallower than the equivalent WIND current sheet spectral slopes.

The occurrence distributions of the 178 spectral slopes for the 178 MMS current sheets are plotted as the dashed curves in Figure 7. The mean values of the distributions are -2.83 for the Gaussian window (blue), -2.78 for the exponential-4 window (red), and -2.75 for the exponential-8 window (cf. Table 1). These MMS current sheet spectral slopes are shallower than the WIND current sheet values.

To put the WIND and MMS magnetic field data on a similar footing, the purple curve in Figure 8 plots the averaged PSD for the 178 individual MMS current sheets after the MMS time series were subjected to 12-point running averages. The time resolutions of the 0.09375-s WIND data and the 7.81×10^{-3} -s MMS data differ by a factor of 12; the 12-point averaging of the MMS data reduce its time resolution to that of the



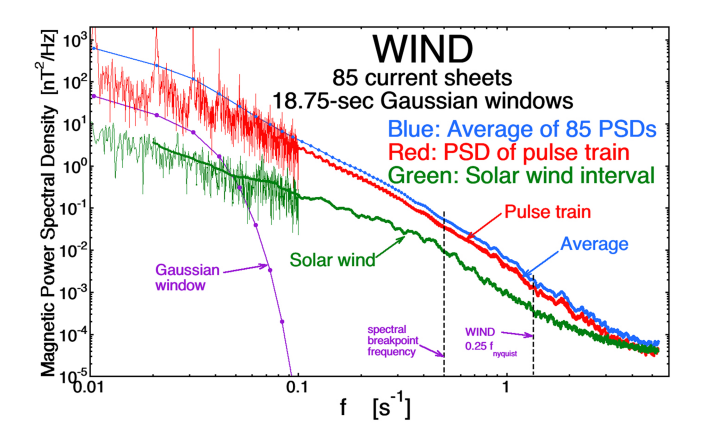


Figure 6. Using a Gaussian window with a halfwidth of 9.375 s, power spectral densities of the WIND current sheets are calculated. The blue curve is the average of the individual power spectral densities of the 85 WIND current sheets. The red curves are the power spectral density of the 85 Gaussian-windowed WIND current sheets sequentially inserted into in a time series. The purple curve is the power spectral density of the 9.375-s Gaussian window. For comparison, the green curve is the magnetic power spectral density of the solar wind as measured by WIND, windowed with a Gaussian with a 51.2-min fullwidth centered on 12 UT on 3 January 2005. The spectral slope of the green solar wind curve is -3.26 in the interval $0.5~{\rm Hz} \leq f \leq 1.33~{\rm Hz}.$

WIND data. The purple curve of Figure 8 shows that the 12-point averaging steepens the spectral slope slightly in the 0.5–1.33 Hz range: For the Gaussian window purple-curve of Figure 8 the spectral slope is –2.88, closer to the values for the WIND current sheets, but not equal to them. The systematic difference between the WIND and MMS spectral slopes is discussed in section 6.1.

The effect of the filter width on the resulting spectral slope is explored in Figure 9. There are six curves for the 178 MMS current sheets and six curves for the 85 WIND current sheets. The blue curves pertain to Gaussian-windowed data, the red curves pertain to exponential-4 windowed data, and the green curves pertain to exponential-8 windowed data. The solid curves are the spectral slopes of log-log power law fits to the average of the set of individual PSDs. One might worry, particularly for the MMS set of current sheets, that current sheets occurring when the total magnetic field strength B_{mag} is large will dominate the averaging of the PSDs (since the PSD is in a sense the square of the magnetic field). To reduce the influence of a few strong-B_{mag} current sheets in the averaging, the dashed curves in Figure 9 utilize averages of normalized PSDs, where all frequency elements of the PSD are divided by the amplitude of the lowest frequency. As can be seen in Figure 9, once the fullwidth of the filter is larger than the thicknesses of the thickest current sheets in the collection (about 10 s), then the spectral slope obtained is fairly insensitive to the width of the filter. The 18.75-s value of the filters used in this study (which

are 100 data points for WIND and 1,200 data points for MMS) is indicated in Figure 9 by the vertical dashed line

The current sheet spectral slopes above the breakpoint seen here are in the range of spectral indices quoted in the literature for the solar wind above the breakpoint that were discussed in section 1. Note that the measured spectral slope of the solar wind above the breakpoint is not a universal value (neither is the spectral slope of the inertial range, which exhibits a variation of values; Borovsky, 2012a; Smith et al., 2006; Tessein et al., 2009; and exhibits systematic differences in the different types of solar wind plasma; Borovsky & Denton, 2010; Borovsky et al., 2019). In Figure 10a the spectral slope in the 0.5-1.33 Hz range is plotted as a function of time in the WIND MFI data set for 3January 2005. A moving window is used to extract a 3.4-hr-long WIND MFI data interval every 1.5 min, and each MFI data interval is windowed with a Gaussian with a 51.2-min full width (red curve) or with a 25.6-min full width (blue curve). The window fullwidths are indicated in Figure 10a with the red and blue horizontal line segments. As can be seen, the resulting high-frequency-1 spectral slope varies with time in the data set from about -2.5 to -5.5, with more variation in the 25.6-min windowing than in the 51.2-min windowing. Note again that the 3 January 2005 WIND data pertains to fast coronal-hole-origin solar wind. In Figure 10c the logarithm of the 10-s change $\Delta\theta_{10-s}$ in the magnetic field direction is plotted. Here, vertical lines indicate the temporal locations of strong current sheets in the WIND MFI time series. Comparing Figures 10a and 10c, there is no easily seen connection between the population of current sheets and the spectral indices. In Figure 10b

Table 1 Spectral Indices for the High-Frequency-1 Range 0.5 Hz \leq f \leq 1.33 Hz for the 85 WIND Current Sheets and the 178 MMS Current Sheets

	Mean of PSDs fits	Fit to sum of PSDs	Fit to sum of normalized PSDs	Fit to PSD of train of 85 current sheets	Fit to sum of PSDs 12-pt-smoothed data	Fit to sum of normalized PSDs 12-pt-smoothed data
WIND Gaussian	3.64	3.36	3.47	3.42		
WIND Exponential-4	3.63	3.35	3.43	3.41		
WIND Exponential-8	3.62	3.34	3.41	3.40		
MMS Gaussian	2.83	2.83	2.97		2.88	3.01
MMS Exponential-4	2.78	2.75	2.92		2.80	2.97
MMS Exponential-8	2.75	2.71	2.89		2.76	2.93



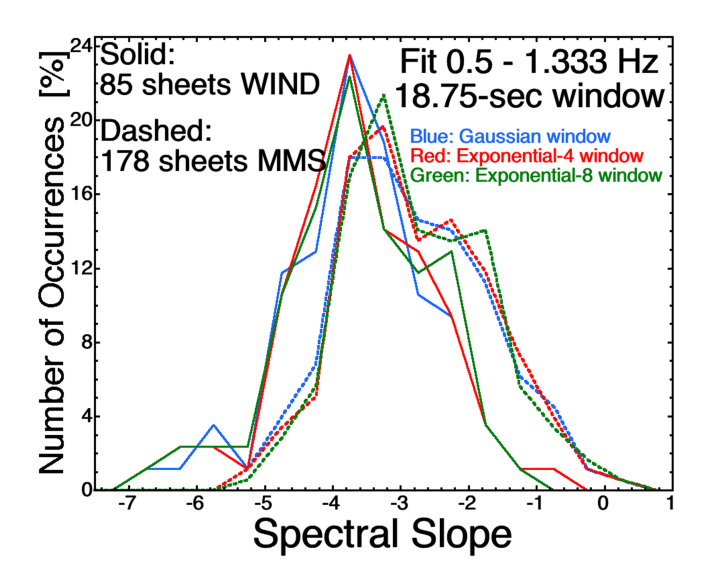


Figure 7. The individual spectral slopes in the frequency range 0.5 Hz \leq f \leq 1.33 Hz are binned for the 85 WIND current sheets (solid curves) and for the 178 MMS current sheets (dashed curves). The blue curves are for power spectral densities calculated using Gaussian windows, the red curves are for exponential-4 windows, and the green curves are for exponential-8 windows.

the relative amplitude of the high-frequency spectrum is plotted (the integral of the PSD from 0.5 Hz to 1.333 Hz, multiplied by a normalization constant so that the normalized amplitude is unity at 12 UT). There is an easily seen connection between the population of strong current sheets in Figure 10c and the spectral amplitude in Figure 10b.

Note in Figure 8 that the MMS power spectra of the 178 current sheets are showing a second breakpoint to shallower spectral slopes in the vicinity of f = 5 Hz. In Figure 11a the MMS power spectra of the current sheets are replotted in blue, red, and green for the Gaussian, the exponential-4, and the exponential-8 windows (all with full widths of 18.75 s) along with three power spectra obtained without windowing. Those three spectra are obtained by linearly detrending the data subinterval that contains each current sheet prior to Fourier transforming (cf. Appendix B of Borovsky, 2012a) and then calculating the 178 PSDs. Each curve is the average of the 178 PSDs. The purple curve takes data subintervals that are 16 s long (with the current sheet at the center of the data subinterval), the gray curve takes data subintervals that are 64 s long, and the orange curve takes data subintervals that are 256 s long. Note the amplitude of magnetic power spectra of the 16-s interval is larger than that of the 64 and the 256 s: This is because a larger fraction of the smaller interval is dominated by the single large current sheet than is the case for the longer intervals. The almost horizontal black dashed curve in Figure 11a is the noise floor of the MMS magnetometer as analyzed by Chhiber et al. (2018); cf.

Figure A1 of that study): This black noise floor pertains to the linear-detrended PSDs of Figure 11a. For the 18.75-s-fullwidth windows, data subintervals with length $L_{\rm FT}=64$ s were Fourier transformed. In this windowing of the 64-s subintervals, about 3/4 of the data (and the noise in the data) in the subinterval is zeroed out. For the Gaussian window the effective width of the window is $\pi^{1/2}$ 9.375 s = 16.6 s, which is 0.26 $L_{\rm FT}$. (For the Exponential4 window the effective length is 0.27 $L_{\rm FT}$ and for the Exponential8 window it is 0.28 $L_{\rm FT}$.) When the Gaussian windowed periodogram that is plotted in Figure 11a was made, the square of the Fourier transform was divided by $L_{\rm FT}$, but the effective length of the Fourier transform is really 0.26 $L_{\rm FT}$. Hence, the actual power of the three windowed curves in Figure 11a is about 4 times what is plotted. To assess the noise for the windowed PSDs in Figure 11a, the (black) noise floor is replotted in blue a factor of 0.26 lower. At 0.25

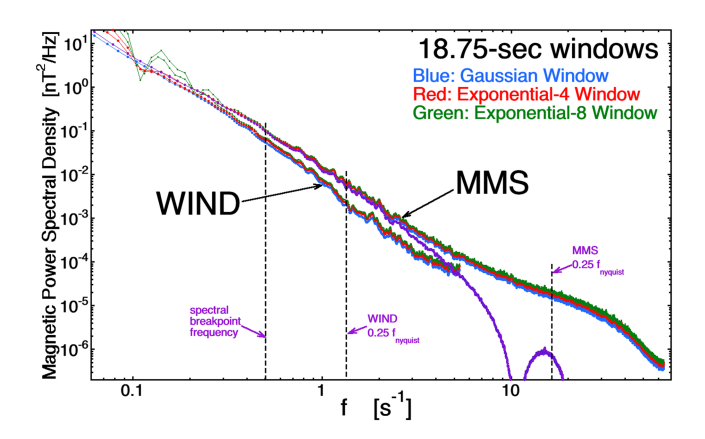


Figure 8. As labeled, the average of the individual magnetic power spectral densities of the 85 WIND current sheets and the 178 MMS current sheets are plotted. The blue curves use Gaussian windowing, the red curves use exponential-4 windowing, and the green curves use exponential-8 windowing. The purple curve is the average power spectral density of the 178 MMS current sheets after 12-point smoothing of the raw MMS data and then Gaussian windowing.

f_{Nyquist} = 16 Hz (vertical black dashed line), and the three windowed PSDs are factors of 18-26 times the (blue) noise floor. At the second breakpoint (~6 Hz, red vertical dashed line), the three windowed PSDs are about a factor of 100 above the (blue) noise floor. These three PSDs are not suffering from instrument noise in the high-frequency-2 range between the second breakpoint and 0.25 $f_{Nyquist}$. At 0.25 $f_{Nyquist}$ the 16-s linear-detrended PSD is a factor of 26 above the (black) noise floor, the 64-s linear-detrended PSD is a factor of 10 above, and the 256-s linear-detrended PSD is only a factor of 2.4 above. For these linear-detrend spectra in Figure 11a it is a mystery as to why the spectra do not flatten in going from 16-s intervals (purple) to 256-s intervals (orange) as the spectral amplitudes approach the (black) noise floor. At the second breakpoint the three linear-detrended curves are factors of 130 (for 16 s), 46 (for 64 s), and 12 (for 256 s) above the (black) noise floor. The 256-s linear-detrended PSD may suffer from instrument noise in the frequency range between the second breakpoint and 0.25 f_{Nyquist}; the other two linear-detrended PSDs probably do not. In Figure 11a the second spectral break is seen in all six of these averaged PSDs. To make the spectral break clearer, the six curves are replotted in Figure 11b as compensated spectra by multiplying by f² before plotting. The three linear-detrended PSDs are also multiplied by a factor of 64 to clearly separate them from the windowed PSDs. In Figure 11b the



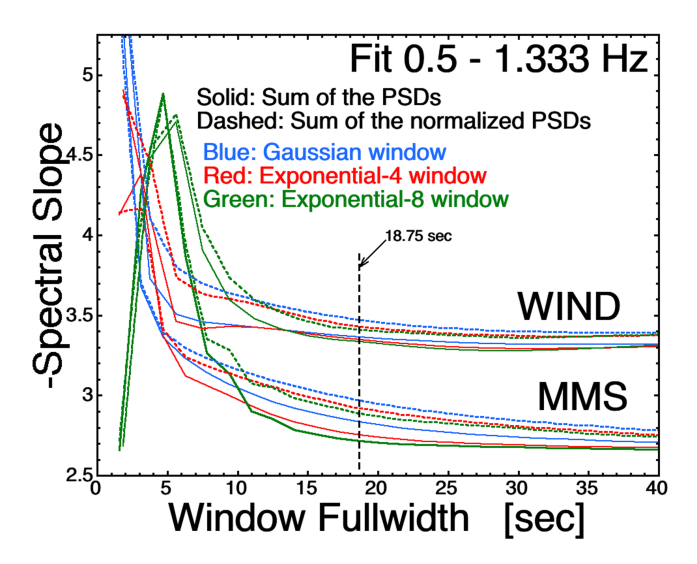


Figure 9. The spectral slopes of the WIND and the MMS current sheets in the frequency range 0.5 Hz $\leq f \leq 1.33$ Hz are plotted versus the fullwidth of the windows used to isolate the current sheet in the solar wind data. The solid curves are the averages of the individual power spectral densities of the sheets, and the dashed curves are the averages of the "normalized" individual power spectral densities. The blue curves are for Gaussian windowing, the red curves for exponential-4 windowing, and the green curves are for exponential-8 windowing. The often-used fullwidth of 18.75 s is noted with the vertical dashed line.

second spectral break (labeled with the red vertical dashed line) at about f=6 Hz is clear. Fitting these averaged magnetic power spectra for the 178 current sheets in the frequency range 8 Hz $\leq f \leq 16$ Hz, spectral slopes of -1.68 for Gaussian, -1.65 for exponential-4, and -1.64 for exponential-8 are obtained. These spectral slopes are shallower than other high-frequency-2 spectral slopes reported in the literature: for example, -2.26 (Podesta, 2010a) or -2.82 (Sahraoui et al., 2010).

In Figure 12, the distribution of spectral slopes in the frequency range 8–16 Hz is binned for the 178 current sheets using Gaussian windows (blue), exponential-4 windows (red), and exponential-8 windows (green), all with 18.75-s fullwidths. The mean value of the spectral-slope distribution is -1.42 for Gaussian, -1.41 for exponential-4, and -1.40 for exponential-8, slightly shallower than the spectral slopes obtained from the fits to the averaged PSDs in Figure 11. The systematic differences between the means of the distributions of spectral slopes and the spectral slope of the sum of the PSDs (previous paragraph) res most likely owed to the fact that summing the spectral slopes treats each event equally, but in the sum of the PSDs spectra with different amplitudes get different weights.

In Figure 13 the fitted spectral slopes of the 178 individual MMS current sheets are plotted as functions of the Pearson linear correlation coefficient $R_{\rm corr}$ of each fitted spectral slope (i.e., for the spectrum of each current sheet it is the correlation between the $\log_{10}(\text{power})$ values and the $\log_{10}(\text{frequency})$ values). The green points are for the blue Gaussian window distribution of Figure 12 (the MMS high-frequency-2 fits), the red points

are for the blue dashed-curve distribution of Figure 7 (the MMS high-frequency-1 fits), and the blue points are for the blue solid-curve distribution of Figure 7 (the WIND high-frequency-1 fits). In all three cases, the pattern of points in Figure 13 is consistent with an underlying spectral slope plus variance error caused by finite data intervals (cf. Figures A2 and A3 of Borovsky, 2012a, and analysis therein).

5. The High-Frequency Fourier Power in the Solar Wind Current Sheets

The question of interest is how much of the high-frequency magnetic spectrum is controlled by strong current sheets in the solar wind. One hint to the answer comes from the three linearly detrended data curves in Figure 11a: As the data interval length is reduced from 256 s (orange), to 64 s (gray), to 16 s (purple), the average power in the data interval increases. This is because the single current sheet in each interval dominates the power over the fluctuations in the solar wind in the vicinity of the current sheet. In going from 256 to 16 s the PSD in the high-frequency range increases by more than a factor of 10.

Comparisons will be made between the magnetic spectral power of solar wind current sheets and the magnetic spectral power of the solar wind, in general.

In Figure 14a the average of the 85 PSDs of the 85 WIND current sheets is plotted in red. Here 24-slong data subintervals containing the current sheets are used and the data subintervals are linearly detrended prior to Fourier transforming. In green in Figure 14a a 3.41-hr-long interval of solar wind (centered on the middle of the day 3 January 2005) is analyzed, with a linear detrend used. (Of course, this 3.41-hr solar wind data interval also has current sheets in it, but not as concentrated as the 85 current sheet intervals.) In the middle of the high-frequency-1 range at $f \sim 0.8$ Hz the red current sheet power spectra are a factor of 7 higher than the solar wind power spectra. An interpretation of this is that one current sheet plus 24 s of solar wind fluctuations has 7 times the power of the ambient solar wind. Hence, a current sheet has as much power, on average, as (7-1)(24 s) = 144 s of solar wind fluctuations. One complication to this is that the background level of fluctuations may be higher in intervals that have current sheets.

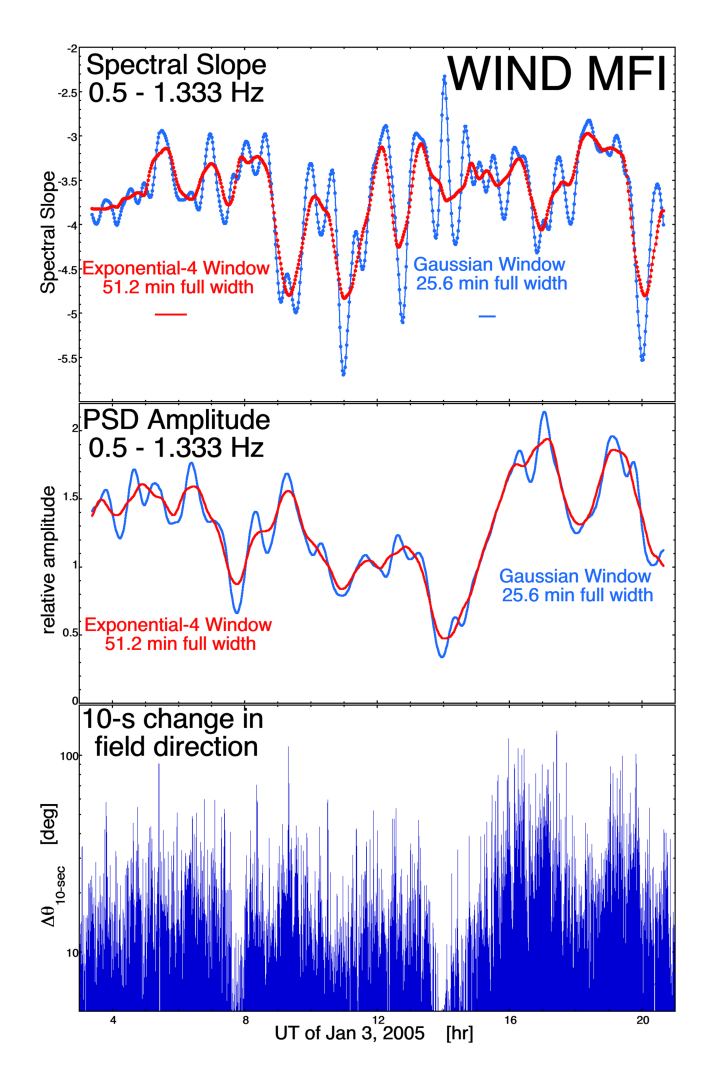


Figure 10. Running Gaussian windows are used on the WIND magnetic field measurement on 3 January 2005 to form running power spectral densities. Power laws are fit to the power spectral densities in the 0.5 Hz $\leq f \leq 1.33$ Hz range of frequencies. In panel (a) the resulting spectral slopes are plotted as functions of time every 1.5 min. The blue curve is for a 25.6-min fullwidth Gaussian window, and the red curve is for a 51.2-min exponential-4 window. In panel (b) the normalized spectral amplitude is plotted for the two windows. Panel (c) plots the logarithm of the 10-s angular change of the magnetic field direction.

A similar measure comes from Figure 14b. Plotted in red is the average of the 85 WIND current sheet PSDs, formed by windowing the data with 18.75-s fullwidth Gaussians. Plotted in green in Figure 14b is the average of 8500 PSD formed by windowing random locations in the 3 January 2005 WIND MFI data set. (And of course, some of these 8,500 random locations have current sheets in them.) At $f \sim 0.8$ Hz the average of the current sheet PSDs is about 5 times the average of the random-location solar wind PSDs. Hence, a current sheet plus 18.75 s of solar wind fluctuations has 4 times the power of 18.75 s of solar wind fluctuations. Accordingly, a current sheet has as much power as (4-1)(18.75 s) = 56 s of ambient solar wind fluctuations. Again, the background level of fluctuations may be higher in intervals that have current sheets.

Also plotted (blue) in Figure 14b is the average PSD of 311 locations in the 3 January 2005 WIND data where there are no strong current sheets. (These locations were selected by visual inspection of plots of the 10-s change in the magnetic field direction, requiring $\Delta\theta_{10\text{-s}}$ to be less than $\sim\!10^{\circ}$ for about 1 min.) At f $\sim\!0.8$ Hz the average amplitude of the current sheet PSDs in Figure 14b is about 13 times the average of the nosheet PSDs.

These two numbers can be compared with the expected occurrence rate of current sheets in the solar wind on 3 January 2005. In Figure 2 the two exponential fits to the $\Delta\theta$ distribution of 3 January (black point) are $206.5\exp(-\Delta\theta/5.84^{\circ})$ for the noncurrent sheet distribution and $4.1\exp(-\Delta\theta/20.2^{\circ})$ for the current sheet distribution. Integrating these two distributions over all values of $\Delta\theta$, the area under the curves is 1,206 for the noncurrent sheet population and 82.9 for the current sheet population. The noncurrent sheet population is 1,206/82.9 = 14.4 times as large as the current sheet population. The 10-s intervals were used to calculate $\Delta\theta$, so current sheets are occurring on the order of every (14.4)(10 s) = 144 s in the fast coronal-hole wind on 3 January. This 144-s occurrence value is on the order of the above 144- and 56-s values for how much solar wind fluctuation is needed to match the power of the current sheets in the high-frequency-1 range. It is plausible that current sheets are accounting for the majority of the power above the spectral breakpoint.

Similar comparisons for MMS can be made by comparing the current sheet PSDs in Figure 11a with the solar wind PSD in Figure A1 of Chhiber et al. (2018). At f=1 Hz the solar wind PSD has an amplitude of $\sim 1 \times 10^{-3}$ nT²/Hz. At f=1 Hz the windowed current sheet PSDs in Figure 11a have a

plotted amplitude of $\sim 1.4 \times 10^{-2} \, \text{nT}^2/\text{Hz}$. Accounting for the effective 16.6-s width of the window in a 64-s data subinterval, the actual amplitude of the windowed current sheet PSDs is $\sim 5.4 \times 10^{-2} \, \text{nT}^2/\text{Hz}$. The short intervals containing current sheets have about 54 times the Fourier power of the typical solar wind of the interval analyzed by Chhiber et al. (2018). The increase in the ratio of Fourier power of MMS versus WIND is almost certainly in part due to the high density of current sheets in fast (coronal-hole-origin) wind (which the WIND analysis of 3January 2005 was) and the fact that the solar wind of the 24 November 2017 (which Chhiber et al., 2018, analyzed) was streamer-belt-origin plasma with a mean speed of 377 km/s.

6. Discussion

6.1. Findings and Implications

This study finds that the high-frequency ($f \ge 0.5$ Hz) magnetic spectrum of isolated solar wind current sheets is consistent with the high-frequency magnetic power spectrum of the solar wind. This can be seen in Figures 6 and 14, or by comparing the high-frequency spectral slopes found here with high-frequency



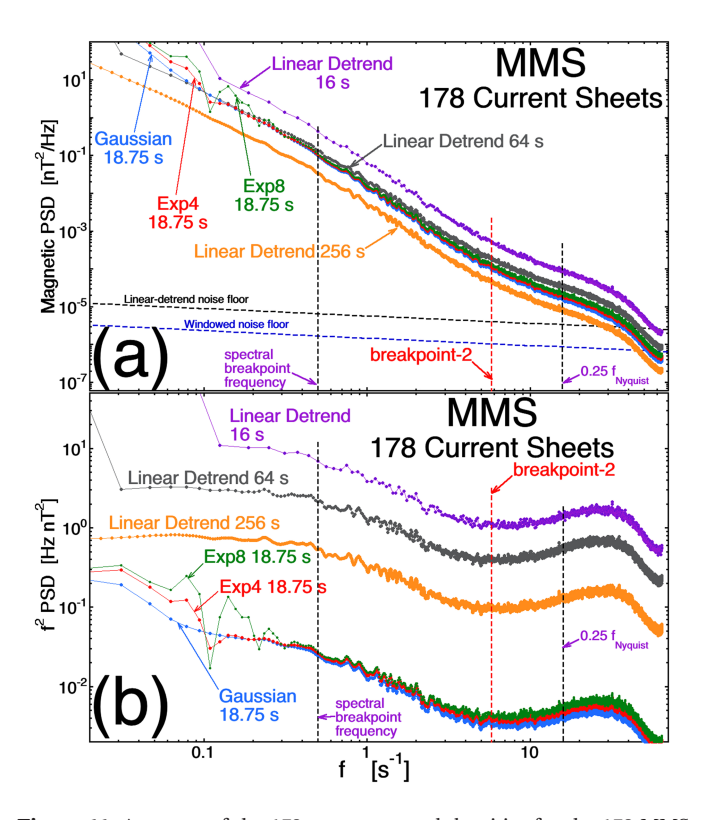


Figure 11. Averages of the 178 power spectral densities for the 178 MMS current sheets are plotted in panel (a) and the averages multiplied by f ² are plotted in panel (b). The blue, red, and green curves are for data windowed with Gaussian, exponential-4, and exponential-8 windows and the purple, gray, and orange curves are for data that is linearly detrended and not windowed. For the linearly detrended power spectral densities the length of the data interval is noted on the plot.

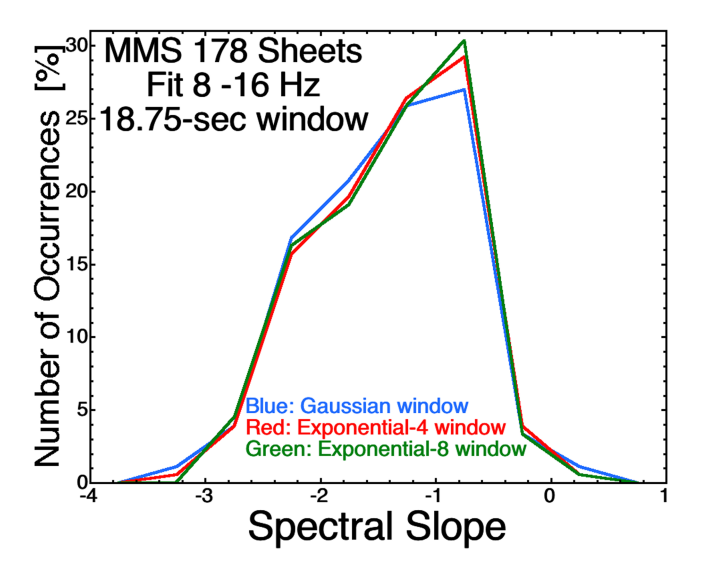


Figure 12. The individual spectral slopes in the frequency range $8 \text{ Hz} \le f \le 16 \text{ Hz}$ are binned for the 178 MMS current sheets. The blue curves are for power spectral densities calculated using Gaussian windows, the red curves are for exponential-4 windows, and the green curves are for exponential-8 windows.

spectral slopes for the solar wind in the literature. From the analysis in sections 3–5 (cf. Figure 5), it is reasonable to suspect that the spatial profile of the current sheets is responsible for the spectral shape of the high-frequency magnetic spectrum of the solar wind.

Systematic differences in the high-frequency spectral slopes are found in this study between the WIND current sheet collection and the MMS current sheet collection (cf. Figure 8 or Table 1). The MMS spectral slopes are closer to the spectral slopes of the 311 no-current sheet intervals. The origins of these differences are not known. The two collections come from different types of solar wind; the WIND current sheets are all from coronal-hole-origin plasma on 3 January 2005, and the MMS current sheets come from diverse types of solar wind plasma. There also might be alteration of the MMS current sheets by foreshock effects.

This study finds that in the high-frequency range $f \ge 0.5$ Hz above the breakpoint, the magnetic spectral power of current sheets in the solar wind could account for the majority of the magnetic spectral power of the solar wind. The Fourier power in the current sheet intervals is several times more intense than typical solar wind intervals, and current sheet occurrence is sufficient to add up to the solar wind's magnetic power. Note, however, that the spectral slope of time intervals without strong current sheets is not drastically different than the spectral slope of current sheets. This raises the question as to whether there are other features in the solar wind magnetic time series that produce spectra similar to the spectra of strong current sheets: perhaps weak current sheets.

The Fourier analysis of MMS current sheets finds a second, shallower, higher-frequency spectrum above 8 Hz, as has been reported for solar wind spectra (e.g., Podesta, 2010a; Sahraoui et al., 2010). The spectral slope of the MMS current sheet higher-frequency spectra is on average shallower than those reported by Podesta, 2010a and Sahraoui et al. (2010); this difference is not understood. Perhaps there may be foreshock contamination of the solar wind current sheets observed by MMS. The noise floor of the MMS magnetometer was investigated, and it was argued in section 4 that the MMS current sheet spectra should not be impacted by noise.

Via a series of studies it has been demonstrated that the current sheets of the solar wind (1) control the amplitude and spectral slope of the inertial range (Borovsky, 2010), (2) control the frequency at which the breakpoint ending the inertial range occurs (Borovsky & Podesta, 2015), and (3) have strong influence on the spectral power and spectral slope of the high-frequency range (the present study). Understanding the origins of the current sheets, the properties of the current sheets, and the physical mechanisms acting on the current sheets are keys to understanding the magnetic power spectrum of the solar wind. A focus on the physics of current sheets could compliment the present focus on a turbulent cascade driving the magnetic spectrum.

This said, the second column of Table 2 lists some concepts needed to fully understand the magnetic spectrum of the solar wind. The standard method for describing the parts of the magnetic power spectrum is via an energy-cascade picture. Sketches of the cascade concept of the solar wind magnetic spectrum can be found in Figure 19 of Goldstein et al. (2015), Figure 2 of Howes (2015), and Figure 14of Matthaeus et al. (2015). The first column of Figure 2 lists the main concepts used in that method of describing the solar wind's magnetic power spectrum. Note



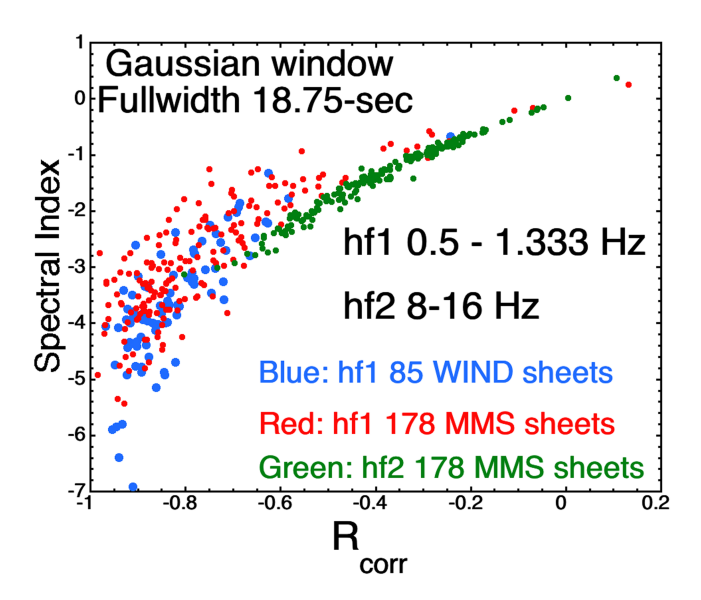


Figure 13. The spectral slopes of the individual current sheets are plotted as a function of the Pearson linear correlation coefficient $R_{\rm corr}$ between the logarithm of the power spectral density and the logarithm of the frequency in the frequency range where the spectral-slope fit is made. The blue points are the 85 WIND current sheets fit in the frequency range $0.5~{\rm Hz} \le f \le 1.33~{\rm Hz}$, the red points are the 178 MMS current sheets fit in the frequency range $0.5~{\rm Hz} \le f \le 1.33~{\rm Hz}$, and the green points are the 178 MMS current sheets fit in the frequency range $6~{\rm Hz} \le f \le 16~{\rm Hz}$.

that the cascade picture does contain current sheets (Greco et al., 2009; Vasquez et al., 2013; Zhdankin et al., 2012), usually described as intermittent structures in the turbulence, and it does consider magnetic field reconnection of those current sheets (Boldyrev & Loureiro, 2017; Karimabadi et al., 2013). The purpose of Table 2 is to highlight the multitude of potential physical processes involved in the physics of the solar wind current sheets.

In a cascade picture, the spectral slope of the inertial range is associated with the nonlinear interaction of MHD magnetic and velocity fluctuations and the transfer of energy from larger-scale fluctuations to smaller-scale fluctuations (Boldyrev, 2006; Goldreich & Sridhar, 1997; Kraichnan, 1965; Podesta, 2010b). Traditionally, it is the spectrum of eddy sizes or the amount of energy in eddies of the various sizes (cf. section 8.3 of Tennekes & Lumley, 1972; section 7.3 of Frisch, 1995; and section 2.9 of Bruno & Carbone, 2016). Finding #1 in Table 2 points out that the amplitude and spectral shape of the inertial range is associated with current sheet amplitudes and recurrence times. As noted in Table 2, for understanding the inertial range, the origin and statistical properties of directional discontinuities (strong current sheets) in the solar wind is important. There are unsettled issues about the origin of these discontinuities (Burkholder & Otto, 2019; Li & Qin, 2011; Neugebauer & Giacalone, 2010, 2015; Owens et al., 2011; Tu et al., 2016) and the role of MHD turbulence, coronal flux tubes, Alfvén waves, pressure-balance structures, mirror modes, etc., in the creation of these current sheets in the solar wind.

In a cascade picture the high-frequency breakpoint of the solar wind magnetic power spectrum is associated with the onset in the MHD cascade of kinetic plasma wave damping (e.g., Bruno & Trenchi, 2014; D'Amicis et al., 2019; Gary, 1999; Gary & Borovsky, 2004, 2008; Howes et al., 2008; Leamon et al., 1998, 1999; Podesta, 2012; Podesta et al., 2010) or with the onset of dispersion of plasma waves (Sahraoui et al., 2010, 2012; Saito et al., 2010; Stawicki et al., 2001; TenBarge et al., 2012). Finding #2 in Table 2 points out that the spectral breakpoint is associated with the thicknesses of current sheets in the solar wind. As noted in Table 2, physical processes that act on the thicknesses of current sheets are important, such as plasma expansion and compression (Schindler & Hesse, 2008, 2010), Bohm and gyro-Bohm diffusion (Borovsky, 2006; Borovsky & Gary, 2009; Pecseli & Mikkelsen, 1985; Perkins et al., 1993; Vahala & Montgomery, 1971), eddy diffusion (Borovsky, 2006; Chen & Montgomery, 1987; Yoshizawa & Yokoi, 1996), Alfvén wave steepening (Tsurutani & Ho, 1999; Vasquez & Hollweg, 2001), current sheet instabilities (Birn et al., 2004; Daughton, 2003; Roytershteyn & Daughton, 2008), and reconnection (Faganello et al., 2010; Gosling & Phan, 2013; Yin & Winske, 2002).

In a cascade picture the high-frequency magnetic power spectrum of the solar wind is associated with plasma wave modes (e.g., whistler waves; Narita & Gary, 2010; Gary et al., 2012; Narita et al., 2016, kinetic Alfvén waves; Podesta & TenBarge, 2012; Smith et al., 2012; Podesta, 2013; Salem et al., 2012; Chen et al., 2013; Pitna et al., 2019), both (Boldyrev et al., 2013; Gary & Smith, 2009; Mithaiwala et al., 2012), and perhaps Bernstein waves (Podesta, 2012; Verscharen et al., 2012), the wave-wave interactions of these plasma modes, and the kinetic damping of these wave modes. In the cascade picture the high-frequency spectrum represents the amplitudes of plasma waves with various wavenumbers. Finding #3 in Table 2 points out that the profiles of solar wind current sheets determine the high-frequency magnetic spectra. As noted in Table 2, physical concepts that are important to the spatial profiles of current sheets are current sheet structuring (Gekelman et al., 2016; Ng et al., 2019; Schindler & Birn, 2002; Schindler & Hesse, 2008), plasma expansion and compression (Schindler & Hesse, 2008, 2010), Bohm and gyro-Bohm diffusion (Borovsky & Gary, 2009; Pecseli & Mikkelsen, 1985; Vahala & Montgomery, 1971), finite-gyroradii effects (Schindler & Hesse, 2010), ion versus electron current carriers (Aunai et al., 2013; Sasunov et al., 2016; Schindler & Birn, 2002), Alfvén wave nonlinear processes (Gomberoff, 2007; Tsurutani et al., 2000), plasma waves in current sheets (Huang et al., 2009; Malaspina et al., 2013; Verscharen & Marsch, 2011; Zelenyi et al., 2011), pressure balance



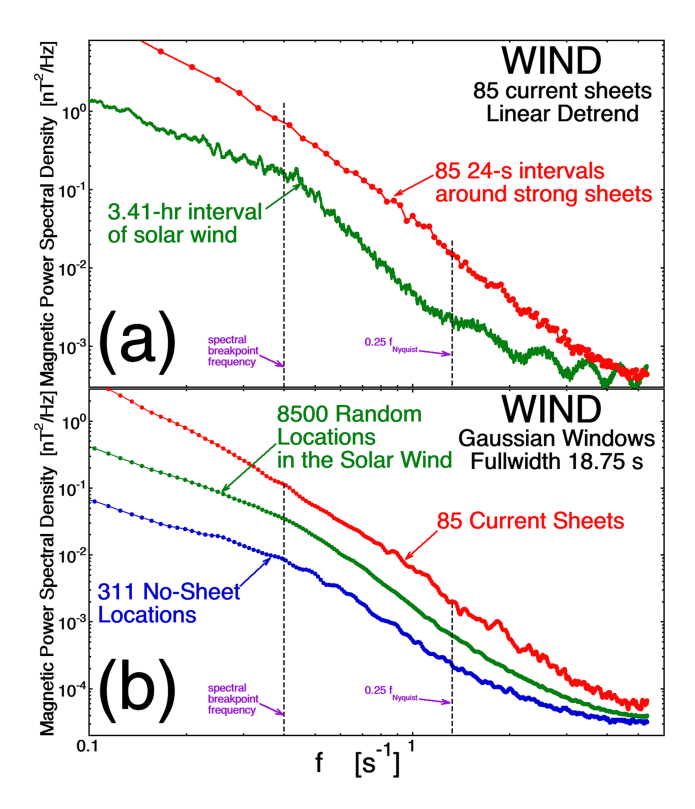


Figure 14. The amplitudes of the magnetic power spectral densities of the WIND current sheets are compared with that of the solar wind. In panel (a) using linear detrending the average of the power spectra of the 85 individual current sheets are plotted in red for 24-s-long data intervals containing the sheets and the power spectra of a 3.21-hr interval of solar wind is plotted in green. In panel (b) using Gaussian windows with a fullwidth of 18.75 s the average of the 85 power spectra of the WIND current sheets are plotted in red, the average of 8,500 power spectra for 8,500 random locations in the solar wind are plotted in green, and the average of 311 locations absent of strong current sheets are plotted in blue.

(Riazantseva et al., 2005; Tu et al., 2016; Zhang et al., 2008), and three-dimensional reconnection (Huang & Bhattacharjee, 2016; Wyper & Hesse, 2015).

6.2. Questions for the Future

To improve and advance the present study of the contribution of solar wind current sheets to the solar wind magnetic spectrum above the breakpoint, several things could be done. Larger collections of current sheets would improve the statistical results and increase the confidence of the interpretations. With larger collections of current sheets, the events could be sorted into categories that are analyzed separately. An obvious sort is into the different types of solar wind plasma (e.g., Neugebauer et al., 2003, 2016; Reisenfeld et al., 2003; Xu & Borovsky, 2015; Zhao et al., 2009): The properties of the solar wind magnetic fluctuations in the inertial range of frequencies show systematic differences between the various origin types of plasma (Borovsky et al., 2019), and it may be the case that the properties of the magnetic spectra above the breakpoint also show systematic differences between the types of solar wind plasma. It is also of interest to sort and separately analyze current sheets according to (1) Alfvénic versus non-Alfvénic current sheets, (2) current sheets with or without changes in the magnetic field strength B_{mag} , and (3) current sheets that are or are not also plasma boundaries. Sorting the current sheet events according to the slant angle at which the spacecraft crosses the current sheet (cf. Figure 7 of Borovsky, 2008) would also improve the numerical values obtained from the analysis. Future high-time-resolution magnetic field measurements far from the bow shock could alleviate issues of the foreshock contamination of solar wind current sheets.

Analogous to the effects of current sheets (magnetic shears) on the magnetic power spectrum of the solar wind, an obvious question for a future study is: What are the effects of sudden velocity shears on the velocity power spectrum of the solar wind? Strong shears in the parallel-to-B flow (velocity shear layers) colocated with current sheets are prevalent in the solar wind plasma (Borovsky, 2012b; Borovsky, 2020b). Particularly in

the Alfvénic regions of the solar wind, the velocity shears $\Delta \underline{v}$ have very similar properties to those of the magnetic shears $\Delta \underline{B}$ (Neugebauer, 1985, 2006; Vasquez et al., 2007). Velocity vector differences in the solar wind have similar statistical properties to those of the magnetic field vector differences (cf. Figure 7 of Salem et al., 2009). And the velocity power spectrum of the solar wind has similarities to the magnetic power spectrum of the solar wind in the inertial range (cf. Figure 6 of Podesta et al., 2007, or Figure 6 of Borovsky, 2012a) and at the breakpoint and above the breakpoint (cf. Figure 1 of Riazantseva et al., 2017, and Figures 1 and 2 of Safrankova et al., 2016). Velocity shear layers can have similar thicknesses as do the colocated magnetic shear layers (cf. Figure 9 of Burkholder and Otto (2019), and in the Alfvénic wind they can have similar amplitudes.

Similar questions arise for other solar wind quantities. (1) What effects do the sudden changes in the magnetic field strength B_{mag} in the solar wind have on the power spectra of B_{mag} for the solar wind? What effects do the sudden changes in the number density n in the solar wind have on the power spectra of the density of the solar wind? (cf. Figure 1 of Safrankova et al., 2013, or Figure 1 of Safrankova et al., 2015).

With the high-frequency spectrum coming from current sheets, and with the high-frequency spectral shape of analytic current sheets coming from discontinuities in the derivatives (cf. Figure 5), an analysis of derivatives in the solar wind time series might be useful. As noted in section 3, discontinuities in the function (the zeroth derivative) give rise to f^{-2} power spectra, discontinuities in the first derivative give rise to f^{-4} spectra, discontinuities in the second derivative give f^{-6} spectra. The pattern is that discontinuities in the nth derivative d^NB/dt^N give rise to power spectra of the form f^{α} where $\alpha = -2(N+1)$. It may be worth exploring the properties of the fractional derivatives of the solar wind time series (e.g., Repperger et al., 2009) to see if they



Table 2

Three Findings About the Importance of Current Sheets in the Solar Wind, the Implications of Those Findings, and New Concepts in Addition to the Concepts of a Purely Cascade Picture of the Solar Wind

Finding 1: Current sheet amplitudes and recurrence times control the inertial-range amplitude and spectral slope

Implication: Understanding the origin of strong current sheets is key to understanding the inertial range

Concepts important to a cascade picture:

Spectrum of eddy sizes

Nonlinear dynamics of eddy-eddy interaction

Spectral anisotropy Intermittent structure

Finding 2: Current sheet thickness determines the breakpoint frequency

Concepts important to a current sheet picture:

Properties of directional discontinuities

Origin of discontinuities Statistics of discontinuities Flux-tube structure

Implication: The physics of what governs the breakpoint frequency is the physics of what governs current sheet thickness

Concepts important to a cascade picture:

Onset of dissipation in the MHD cascade

Transition from MHD to kinetic Landau and cyclotron resonances

Mode conversion

Reconnection

Concepts important to a current sheet

picture:

Plasma expansion and compression

Bohm diffusion Eddy diffusion

Alfvén wave steepening Current sheet instabilities

Reconnection Solar wind evolution

Finding 3: Current sheet profile determines the spectral slope above the breakpoint

Implication: Physical mechanisms acting within current sheets should be investigated to understand the high-frequency spectra of the solar wind

Concepts important to a cascade picture:

Dispersion relations

Wave-wave interactions

Landau and cyclotron damping

Anisotropy spectra

Concepts important to a current sheet

picture:

Current sheet structuring

Plasma expansion and compression Bohm and gyro-Bohm diffusion Finite-gyroradius effects

Ion versus electron current carriers Alfvén wave nonlinear processes Plasma waves in current sheets

Pressure balance

Three-dimensional reconnection

Acknowledgments

The authors wish to thank John Podesta and Chuck Smith for useful conversations. Work at the Space Science Institute was supported by the NASA Heliophysics Guest Investigator Program via Grant NNX17AB71G, by the NSF SHINE program via Award AGS-1723416, by the NASA Heliophysics LWS program via Grant NNX16AB75G, and by the NSF GEM Program. Work at Embry-Riddle Aeronautical University was supported by the NASA Heliophysics Guest Investigator program by via Grant NASA H-GI 80NSSC18K1381. All WIND and MMS data sets utilized are available at the NASA Space Physics Data Facility https://cdaweb.gsfc.nasa. gov, and current sheet event lists are available in the Zenodo public data repository at https://doi.org/10.5281/ zenodo.3595588.

can provide insight into the noninteger high-frequency power laws observed in the PSDs. Fractional derivatives of the time series are readily calculated using Fourier transforms (Meerschaert et al., 2014; Tseng et al., 2000).

Since the current sheets of the solar wind are playing such a strong role, and since the physical processes in the current sheets must be important, future studies and future measurements should focus on high-timeresolution measurements of waves and particle distribution functions within the solar wind current sheets.

References

Alexandrova, O., Saur, J., Lacombe, C., Mangeney, A., Mitchell, J., Schwartz, S. J., & Robert, P. (2009). Universality of solar-wind turbulent spectrum from MHD to electron scales. Physical Review Letters, 103, 165003. https://doi.org/10.1103/PhysRevLett.103.165003 Aunai, N., Belmont, G., & Smets, R. (2013). First demonstration of an asymmetric kinetic equilibrium for a thin current sheet. Physics of Plasmas, 20, 110702. https://doi.org/10.1063/1.4833679

Birn, J., Dorelli, J. C., Hesse, M., & Schindler, K. (2004). Thin current sheets and loss of equilibrium: Three-dimensional theory and simulation. Journal of Geophysical Research, 109, A02215. https://doi.org/10.1029/2003JA010275

Boldyrev, S. (2006). Spectrum of magnetohydrodynamic turbulence. Physical Review Letters, 96, 115002. https://doi.org/10.1103/ PhysRevLett.96.115002

Boldyrev, S., Horaites, K., Xia, Q., & Perez, J. C. (2013). Toward a theory of astrophysical plasma turbulence at subproton scales. The Astrophysical Journal, 777(1), 41. https://doi.org/10.1088/0004-637X/777/1/41



- Boldyrev, S., & Loureiro, N. F. (2017). Magnetohydrodynamic turbulence mediated by reconnection. *The Astrophysical Journal*, 844, 124. https://doi.org/10.3847/1538-4357/aa7d0
- Borovsky, J. E. (2006). The eddy viscosity and flow properties of the solar wind: CIRs, CME sheaths, and solar-wind/magnetosphere coupling. *Physics of Plasmas*, 13, 056505. https://doi.org/10.1063/1.2200308
- Borovsky, J. E. (2008). The flux-tube texture of the solar wind: Strands of the magnetic carpet at 1 AU? *Journal of Geophysical Research*, 113, A08110. https://doi.org/10.1029/2007JA012684
- Borovsky, J. E. (2010). On the contribution of strong discontinuities to the power spectrum of the solar wind. *Physical Review Letters*, 105, 111102. https://doi.org/10.1103/PhysRevLett.105.111102
- Borovsky, J. E. (2012a). The velocity and magnetic-field fluctuations of the solar wind at 1 AU: Statistical analysis of Fourier spectra and correlations with plasma properties. *Journal of Geophysical Research*, 117, A05104. https://doi.org/10.1029/2011JA017499
- Borovsky, J. E. (2012b). The effect of sudden wind shear on the Earth's magnetosphere: Statistics of wind-shear events and CCMC simulations of magnetotail disconnections. *Journal of Geophysical Research*, 117, A06224. https://doi.org/10.1029/2012JA017623
- Borovsky, J. E. (2020a). The magnetic structure of the solar wind: Ionic composition and the electron strahl. *Geophysical Research Letters*, 46. https://doi.org/10.1029/2019GL084586
- Borovsky, J. E. (2020b). On the motion of the heliospheric magnetic structure through the solar wind plasma. *Journal of Geophysical Research: Space Physics*, 125, e2019JA027377. https://doi.org/10.1029/2019JA027307
- Borovsky, J. E., & Denton, M. H. (2010). Solar-wind turbulence and shear: A superposed-epoch analysis of corotating interaction regions at 1 AU. *Journal of Geophysical Research*, 115, A10101. https://doi.org/10.1029/2009JA014966
- Borovsky, J. E., Denton, M. H., & Smith, C. W. (2019). Some properties of the solar-wind turbulence at 1 AU statistically examined in the different types of solar-wind plasma. *Journal of Geophysical Research*, 124, 2406–2424. https://doi.org/10.1029/2019JA026580
- Borovsky, J. E., & Gary, S. P. (2009). On viscosity and the Reynolds number of MHD turbulence in collisionless plasmas: Coulomb collisions, Landau damping, and Bohm diffusion. *Physics of Plasmas*, 16, 082307. https://doi.org/10.1063/1.3155134
- Borovsky, J. E., & Podesta, J. J. (2015). Exploring the effect of current-sheet thickness on the high-frequency Fourier spectrum of the solar wind. *Journal of Geophysical Research: Space Physics*, 120, 9256–9268. https://doi.org/10.1002/2015JA021622
- Bruno, R., & Carbone, V. (2016). Turbulence in the solar wind. In *Lecture Notes in Physics*, (Vol. 928, pp. 78–83). Switzerland: Springer International Publishing.
- Bruno, R., Telloni, D., DeIure, D., & Pietropaolo, E. (2017). Solar wind magnetic field background spectrum from fluid to kinetic scales. Monthly Notices of the Royal Astronomical Society, 472(1), 1052–1059. https://doi.org/10.1093/mnras/stx2008
- Bruno, R., & Trenchi, L. (2014). Radial dependence of the frequency break between fluid and kinetic scales in the solar wind fluctuations. The Astrophysical Journal Letters, 787, L24. https://doi.org/10.1088/2041-8205/787/2/L24
- Burkholder, B. L., & Otto, A. (2019). Magnetic reconnection of solar flux tubes and coronal reconnection signatures in the solar wind at 1 AU. *Journal of Geophysical Research: Space Physics*, 124, 8227–8254. https://doi.org/10.1029/2019JA027114
- Chen, C. H. K., Boldyrev, S., Xia, Q., & Perez, J. C. (2013). The nature of subproton scale turbulence in the solar wind. *Physical Review Letters*, 110, 225002. https://doi.org/10.1103/PhysRevLett.110.225002
- Chen, C. H. K., Leung, L., Boldyrev, S., Maruca, B. A., & Bale, S. D. (2014). Ion-scale spectral break of solar wind turbulence at high and low beta. *Geophysical Research Letters*. 41, 8081–8088, https://doi.org/10.1002/2014GL062009
- Chen, H., & Montgomery, D. (1987). Turbulent MHD transport coefficients: An attempt at self-consistency. Plasma Physics and Controlled Fusion, 29(2), 205–226. https://doi.org/10.1088/0741-3335/29/2/006
- Chhiber, R., Chasapis, A., Bandyopadhyay, R., Parashar, T. N., Matthaeus, W. H., Maruca, B. A., et al. (2018). Higher-order turbulence statistics in the Earth's magnetosheath and the solar wind using Magnetospheric Multiscale observations. *Journal of Geophysical Research: Space Physics*, 123, 9941–9954. https://doi.org/10.1029/2018JA025768
- Coleman, P. J. (1968). Turbulence, viscosity, and dissipation in the solar-wind plasma. The Astrophysical Journal, 153, 371. https://doi.org/ 10.1086/149674
- D'Amicis, R., Matteini, L., & Bruno, R. (2019). On the slow solar wind with high Alfvénicity: From composition and microphysics to spectral properties. *Monthly Notices of the Royal Astronomical Society*, 483, 4665–4677. https://doi.org/10.1093/mnras/stv3320
- Daughton, W. (2003). Electromagnetic properties of the lower-hybrid drift instability in a thin current sheet. *Physics of Plasmas*, 10(8), 3103–3119. https://doi.org/10.1063/1.1594724
- Faganello, M., ZPegoraro, F., Califano, F., & Marradi, L. (2010). Collisionless magnetic reconnection in the presence of a sheared velocity field. *Physics of Plasmas*, 17, 062102. https://doi.org/10.1063/1.3430640
- Frisch, U. (1995). Turbulence. Cambridge: Cambridge, University Press.
- Gary, S. P. (1999). Collisionless dissipation wavenumber: Linear theory. *Journal of Geophysical Research*, 104(A4), 6759–6762. https://doi.org/10.1029/1998JA900161
- Gary, S. P., & Borovsky, J. E. (2004). Alfvén-cyclotron fluctuations: Linear Vlasov theory. Journal of Geophysical Research, 109, A06105. https://doi.org/10.1029/2004JA010399
- Gary, S. P., & Borovsky, J. E. (2008). Damping of long-wavelength kinetic Alfvén fluctuations: Linear theory. *Journal of Geophysical Research*, 109, A12104. https://doi.org/10.1029/2004JA010399
- Gary, S. P., Chang, O., & Wang, J. (2012). Forward cascade of whistler turbulence: Three-dimensional particle-in-cell simulations. The Astrophysical Journal, 755, 142. https://doi.org/10.1088/0004-637X/755/2/142
- Gary, S. P., & Smith, C. W. (2009). Short-wavelength turbulence in the solar wind: Linear theory of whistler and kinetic Alfvén fluctuations. Journal of Geophysical Research, 114, A12105. https://doi.org/10.1029/2009JA014525
- Gekelman, W., DeHaas, T., Van Compernolle, B., Daughton, W., Pribyl, P., Vicena, S., & Hong, D. (2016). Experimental study of the dynamics of a thin current sheet. *Physica Scripta*, 91, 054002. https://doi.org/10.1088/0031-8949/91/5/054002
- Goldreich, P., & Sridhar, S. (1997). Magnetohydrodynamic turbulence revisited. Astrophysical Journal, 485(2), 680–688. https://doi.org/ 10.1086/304442
- Goldstein, M. L., Escoubet, P., Hwang, K. J., Wendel, D. E., Vinas, A.-F., Fung, S. F., et al. (2015). Multipoint observations of plasma phenomena made in space by Cluster. *Journal of Plasma Physics*, 81, 325810301. https://doi.org/10.1017/ S0022377815000185
- Gomberoff, L. (2007). Parametric decays, stabilization effects, and electrostatic instabilities due to finite-amplitude Alfvén waves in a fast solar wind-like plasma. Journal of Geophysical Research, 112, A10108. https://doi.org/10.1029/2007JA012529
- Gosling, J. T., & Phan, T. D. (2013). Magnetic reconnection in the solar wind at current sheets associated with extremely small field shear angles. The Astrophysical Journal Letters, 763, L39. https://doi.org/10.1088/2041-8205/763/2/L39

BOROVSKY AND BURKHOLDER 15 of 18



- Greco, A., Matthaeus, W. H., Servidio, S., Chuychai, P., & Dmitruk, P. (2009). Statistical analysis of discontinuities in solar wind ACE data and comparison with intermittent MHD turbulence. *Astrophysical Journal*, 691(2), 111–114. https://doi.org/10.1088/0004-637X/691/2/L111
- Howes, G. G. (2015). A dynamical model of plasma turbulence in the solar wind. *Philosophical Transactions of the Royal Society*, 373, 20140145. https://doi.org/10.1098/rsta.2014.0145
- Howes, G. G., Cowley, S. C., Dorland, W., Hammett, G. W., Quataert, E., & Schekochihin, A. A. (2008). A model of turbulence in magnetized plasmas: Implications for the dissipation range in the solar wind. *Journal of Geophysical Research*, 113, A05103. https://doi.org/10.1029/2007JA012665
- Huang, F., Chen, Y., Shi, G., Hu, Z., Peng, H., Zheng, J., & Yu, M. Y. (2009). Lower-hybrid drift instability in a thin current sheet with κ velocity distribution. *Physics of Plasmas*, 16, 042107. https://doi.org/10.1063/1.3116643
- Huang, Y.-M., & Bhattacharjee, A. (2016). Turbulent magnetohydrodynamic reconnection mediated by the plasmoid instability. The Astrophysical Journal, 818, 20. https://doi.org/10.3847/0004-637X/818/1/20
- Karimabadi, H., Roytershteyn, V., Wan, M., Matthaeus, W. H., Daughton, W., Wu, P., et al. (2013). Coherent structures, intermittent turbulence, and dissipation in high-temperature plasmas. *Physics of Plasmas*, 20, 012303. https://doi.org/10.1063/1.4773205
- Kraichnan, R. H. (1965). Inertial-range spectrum of hydromagnetic turbulence. *Physics of Fluids*, 8(7), 1385–1387. https://doi.org/10.1063/1.1761412
- Leamon, R. J., Smith, C. W., Ness, N. F., Matthaeus, W. H., & Wong, H. K. (1998). Observational constraints on the dynamics of the interplanetary magnetic field dissipation range. *Journal of Geophysical Research*, 103(A3), 4775–4787. https://doi.org/10.1029/97JA03394
- Leamon, R. J., Smith, C. W., Ness, N. F., & Wong, H. K. (1999). Dissipation range dynamics: Kinetic Alfvén waves and the importance of β_e. Journal of Geophysical Research, 104(A10), 22,331–22,344. https://doi.org/10.1029/1999JA900158
- Lepping, R. P., Acuna, M. H., Burlaga, L. F., Farrell, W. M., Slavin, J. A., Schatten, K. H., et al. (1995). The WIND magnetic field investigation. Space Science Reviews, 71(1-4), 207–229. https://doi.org/10.1007/BF00751330
- Li, G., Miao, B., Hu, Q., & Qin, G. (2011). Effect of current sheets on the solar wind magnetic field power spectrum from the Ulysses observation: From Kraichnan to Kolmogorov scaling. *Physical Review Letters*, 106, 125001. https://doi.org/10.1103/ PhysRevLett.106.125001
- Li, G., & Qin, G. (2011). A realistic solar wind model with current sheets. In N. V. Pogorelov, E. Audit, & G. P. Zank (Eds.), Proceedings of 5th Astrophysics Numerical Conference, Numerical Modeling of Space Plasma Flows: ASTRONUM-2010, ASP Conference Series (Vol. 444, pp. 117–123). Bristol, UK: IOP Publishing Ltd.
- Li, G., Qin, G., Hu, Q., & Miao, B. (2012). Effect of current sheets on the power spectrum of the solar wind magnetic field using a cell model. Advances in Space Research, 49(9), 1327–1332. https://doi.org/10.1016/j.asr.2012.02.008
- Malaspina, D. M., Newman, D. L., Wilson, L. B., Goetz, K., Kellogg, P. J., & Kerstin, K. (2013). Electrostatic solitary waves in the solar wind: Evidence for instability at solar wind current sheets. *Journal of Geophysical Research: Space Physics*, 118, 591–599. https://doi.org/10.1002/jgra.50102
- Matthaeus, W. H., Wan, M., Servidio, S., Greco, A., Osman, K. T., Oughton, S., & Dmitruk, P. (2015). Intermittency, nonlinear dynamics and dissipation in the solar wind and astrophysical plasmas. *Philosophical Transactions of the Royal Society*, A373, 20140154. https://doi.org/10.1098/rsta.2014.0154
- Meerschaert, M. M., Sabzikar, F., Phanikumar, M. S., & Zeleke, A. (2014). Tempered fractional time series model for turbulence in geophysical flows. *Journal of Statistical Mechanics: Theory and Experiment*, 2014, P09023. https://doi.org/10.1088/1742-5468/2014/09/P09023
- Miao, B., Peng, B., & Li, G. (2011). Current sheets from Ulysses observation. Annales Geophysicae, 29(2), 237–249. https://doi.org/10.5194/angeo-29-237-2011
- Mithaiwala, M., Rudakov, L., Crabtee, C., & Ganguli, G. (2012). Co-existence of whistler waves with kinetic Alfvén wave turbulence for the high-beta solar wind plasma. *Physics of Plasmas*, 19, 102902. https://doi.org/10.1063/1.4757638
- Narita, Y., & Gary, S. P. (2010). Inertial-range spectrum of whistler turbulence. *Annales Geophysicae*, 28(2), 597–601. https://doi.org/10.5194/angeo-28-597-2010
- Narita, Y., Nakamura, R., Baumjohann, W., Glassmeier, K.-H., Motschmann, U., Giles, B., et al. (2016). On electron-scale whistler turbulence in the solar wind. The Astrophysical Journal Letters, 827, L8. https://doi.org/10.3847/2041-8205/827/1/L8
- Neugebauer, M. (1985). Alignment of velocity and field changes across tangential discontinuities in the solar wind. *Journal of Geophysical Research*, 90, 6627. https://doi.org/10.1029/JA090iA07p06627
- Neugebauer, M.~(2006).~Comment~on~the~abundances~of~rotational~and~tangential~discontinuities~in~the~solar~wind. Journal of Geophysical Research,~111,~A04103.~https://doi.org/10.1029/2005JA011497
- Neugebauer, M., & Giacalone, J. (2010). Progress in the study of interplanetary discontinuities. *AIP Conference Proceedings, 1216*, 194. Neugebauer, M., & Giacalone, J. (2015). Energetic particles, tangential discontinuities, and solar flux tubes. *Journal of Geophysical Research: Space Physics, 120*, 8281–8287. https://doi.org/10.1002/2015JA021632
- Neugebauer, M., Reisenfeld, D., & Richardson, I. G. (2016). Comparison of algorithms for determination of solar wind regimes. *Journal of Geophysical Research: Space Physics*, 121, 8215–8227. https://doi.org/10.1002/2016JA023142
- Neugebauer, M., Steinberg, J. T., Tokar, R. L., Barraclough, B. L., Dors, E. E., Weins, R. C., et al. (2003). Genesis on-board determination of the solar wind flow regime. Space Science Reviews, 105(3/4), 661–679. https://doi.org/10.1023/A:1024478129261
- Ng, J., Hakim, A., Juno, J., & Bhattacharjee, A. (2019). Drift instabilities in thin current sheets using a two-fluid model with pressure tensor effects. *Journal of Geophysical Research: Space Physics*, 124, 3331–3346. https://doi.org/10.1029/2018JA026313
- Otnes, R. K., & Enochson, L. (1972). Digital time series analysis. New York: Wiley.
- Owens, M. J., Wicks, R. T., & Horbury, T. S. (2011). Magnetic discontinuities in the near-Earth solar wind: Evidence of in-transit turbulence or remnants of coronal structure? Solar Physics, 269(2), 411–420. https://doi.org/10.1007/s11207-010-9695-0
- Pecseli, H. L., & Mikkelsen, T. (1985). Turbulent diffusion in two-dimensional, strongly magnetized plasmas. *Journal of Plasma Physics*, 34(1), 77–94. https://doi.org/10.1017/S0022377800002695
- Perkins, F. W., Barnes, C. W., Hohnson, D. W., Scott, S. D., et al. (1993). Nondimensional transport scaling in the Tokamak Fusion Test Reactor: Is tokamak transport Bohm or gyro-Bohm? *Physics of Fluids B*, 5(2), 477–498. https://doi.org/10.1063/1.860534
- Pitna, A., Safrankova, J., Nemecek, Z., Franci, L., Pi, G., & Camps, V. M. (2019). Characteristics of solar wind fluctuations at and below ion scales. *The Astrophysical Journal*, 879(2), 82. https://doi.org/10.3847/1538-4357/ab22b8
- Podesta, J. J. (2010a). Solar wind turbulence: Advances in observation and theory. Advances in Plasma Astrophysics, Proceedings of IAU Symposium, 274, 295.

BOROVSKY AND BURKHOLDER 16 of 18



- Podesta, J. J. (2010b) Theory of solar wind turbulence with scale-dependent alignment, anisotropy, and cross-helicity. AIP Conference Series, 1216, 115.
- Podesta, J. J. (2012). The need to consider ion Bernstein waves as a dissipation channel of solar wind turbulence. *Journal of Geophysical Research*, 117, A07101. https://doi.org/10.1029/2012JA017770
- Podesta, J. J. (2013). Evidence of kinetic Alfvén waves in the solar wind at 1 AU. Solar Physics, 286(2), 529–548. https://doi.org/10.1007/s11207-013-0258-7
- Podesta, J. J. (2016). Spectra that behave like power-laws are not necessarily power-laws. Advances in Space Research, 57, 1127–1132.
- Podesta, J. J., & Borovsky, J. E. (2016). Relationship between the durations of jumps in solar wind time series and the frequency of the spectral break. *Journal of Geophysical Research: Space Physics*, 121, 1817–1838. https://doi.org/10.1002/2015JA021987
- Podesta, J. J., Borovsky, J. E., & Gary, S. P. (2010). A kinetic Alfvén wave cascade subject to collisionless damping cannot reach electron scales in the solar wind at 1 AU. The Astrophysical Journal, 712(1), 685–691. https://doi.org/10.1088/0004-637X/712/1/685
- Podesta, J. J., Roberts, D. A., & Goldstein, M. L. (2007). Spectral exponents of kinetic and magnetic energy spectra in solar wind turbulence. The Astrophysical Journal, 664(1), 543–548. https://doi.org/10.1086/519211
- Podesta, J. J., & TenBarge, J. M. (2012). Scale dependence of the variance anisotropy near the proton gyroradius scale: Additional evidence for kinetic Alfvén waves in the solar wind at 1 AU. *Journal of Geophysical Research*, 117, A10106. https://doi.org/10.1029/ 2012JA017724
- Reisenfeld, D. B., Steinberg, J. T., Barraclough, B. L., Dors, E. E., Weins, R. C., Neugebauer, M., et al., (2003). Comparison of the Genesis solar wind regime algorithm results with solar wind composition observed by ACE, AIP Conference Proceedings, 679, 632.
- Repperger, D. W., Farris, K. A., Barton, C. C., & Tebbens, S. (2009). Time series data analysis using fractional calculus concepts and fractional analysis. Proceedings of the 2009 IEEE International Conference on Systems, Man, and Cypernetics, pg. 3311-3315, IEEE, New York.
- Riazantseva, M. O., Budaev, V., Rakhmanova, L., Zastenker, G., Yermolaev, Y., Lodkina, I., et al. (2017). Variety of shapes of solar wind ion flux spectra: Spektr-R measurements. *Journal of Plasma Physics*, 83(4), 705830401.
- Riazantseva, M. O., Khabarova, O. V., Zastenker, G. N., & Richardson, J. D. (2005). Sharp boundaries of solar wind plasma structures and an analysis of their pressure balance. *Cosmic Research*, 43(3), 157–164. https://doi.org/10.1007/s10604-005-0030-8
- Roytershteyn, V., & Daughton, W. (2008). Collisionless instability of thin current sheets in the presence of sheared parallel flows. *Physics of Plasmas*, 15(8), 082901. https://doi.org/10.1063/1.2968459
- Russell, C. T., Anderson, B. J., Baumjohann, W., Bromund, K. R., Dearborn, D., Fischer, D., et al. (2016). The Magnetospheric Multiscale magnetometers. *Space Science Reviews*, 199(1-4), 189–256. https://doi.org/10.1007/s11214-014-0057-3
- Safrankova, J., Nemecek, Z., Nemec, F., Prech, L., Chen, C. H. K., & Zastenker, G. N. (2016). Power spectral density of fluctuations of bulk and thermal speeds in the solar wind. *The Astrophysical Journal*, 825(2), 121. https://doi.org/10.3847/0004-637X/825/2/121
- Safrankova, J., Nemecek, Z., Nemec, F., Prech, L., Pitna, A., Chen, C. H. K., & Zastenker, G. N. (2015). Solar wind density spectra around the ion spectral break. *The Astrophysical Journal*, 803(2), 107. https://doi.org/10.1088/0004-637X/803/2/107
- Safrankova, J., Nemecek, Z., Prech, L., & Zastenker, G. (2013). Ion kinetic scale in the solar wind observed. *Physical Review Letters*, 110(2), 025004. https://doi.org/10.1103/PhysRevLett.110.025004
- Sahraoui, F., Belmont, G., & Goldstein, M. L. (2012). New insight into short-wavelength solar wind fluctuations from Vlasov theory. *The Astrophysical Journal*, 748(2), 100. https://doi.org/10.1088/0004-637X/748/2/100
- Sahraoui, F., Goldstein, M. L., Belmont, G., Canu, P., & Rezeau, L. (2010). Three dimensional anisotropic k spectra of turbulence at sub-proton scales in the solar wind. *Physical Review Letters*, 105(13), 131101. https://doi.org/10.1103/PhysRevLett.105.131101
- Saito, S., Gary, S. P., & Narita, Y. (2010). Wavenumber spectrum of whistler turbulence: Particle-in-cell simulation. *Physics of Plasmas*, 17(12), 122316. https://doi.org/10.1063/1.3526602
- Salem, C., Mangeney, A., Bale, S. D., & Veltri, P. (2009). Solar wind MHD turbulence: Anomalous scaling and role of intermittency. *The Astrophysical Journal*, 702(1), 537–553. https://doi.org/10.1088/0004-637X/702/1/537
- Salem, C. S., Howes, G. G., Sundkvist, D., Bale, S. D., Caston, C. C., Chen, C. H. K., & Mozer, F. S. (2012). Identification of kinetic Alfvén wave turbulence in the solar wind. *The Astrophysical Journal Letters*, 745(1), L9. https://doi.org/10.1088/2041-8205/745/1/L9
- Sasunov, Y. L., Khodachenko, M. L., Alexeev, I. I., Belenkaya, E. S., Mingalev, O. V., & Melnik, M. N. (2016). The influence of kinetic effect on the MHD scalings of a thin current sheet. *Journal of Geophysical Research: Space Physics*, 122, 493–500. https://doi.org/10.1002/2016JA023162
- Schindler, K., & Birn, J. (2002). Models of two-dimensional embedded thin current sheets from Vlasov theory. *Journal of Geophysical Research*, 107(A8), 1193. https://doi.org/10.1029/2001JA000304
- Schindler, K., & Hesse, M. (2008). Formation of thin bifurcated current sheets by quasisteady compression. *Physics of Plasmas*, 15, 042902. Schindler, K., & Hesse, M. (2010). Conditions for the formation of nongyrotropic current sheets in slowly evolving plasmas. *Physics of Plasmas*, 17, 082103.
- Siscoe, G. L., Davis, L., Coleman, P. J., Smith, E. J., & Jones, D. E. (1968). Power spectra and discontinuities of the interplanetary magnetic field: Mariner 4. *Journal of Geophysical Research*, 73, 61.
- Smith, C. W., Hamilton, K., Vasquez, B. J., & Leamon, R. J. (2006). Dependence of the dissipation range spectrum of interplanetary magnetic fluctuations on the rate of energy cascade. *The Astrophysical Journal*, 645, L85.
- Smith, C. W., Vasquez, B. J., & Hollweg, J. V. (2012). Observational constraints on the role of cyclotron damping and kinetic Alfvén waves in the solar wind. *The Astrophysical Journal*, 745, 8.
- Stawicki, O., Gary, S. P., & Li, H. (2001). Solar wind magnetic fluctuation spectra: Dispersion and damping. *Journal of Geophysical Research*, 106, 8273.
- TenBarge, J. M., Podesta, J. J., Klein, K. G., & Howes, G. G. (2012). Interpreting magnetic variance anisotropy measurements in the solar wind. *The Astrophysical Journal*. 735, 107.
- Tennekes, H., & Lumley, J. L. (1972). A first course in turbulence. Cambridge Massachusetts: MIT Press.
- Tessein, J. A., Smith, C. W., MacBride, B. T., Matthaeus, W. H., Forman, M. A., & Borovsky, J. E. (2009). Spectral indices for multi-dimensional interplanetary turbulence at 1 AU. *The Astrophysical Journal*, 692, 684.
- Tseng, C.-C., Pei, S.-C., & Hsia, S. C. (2000). Computation of fractional derivatives using Fourier transform and digital FIR differentiator. Signal Processing, 80, 151.
- Tsurutani, B. T., Dasgupta, B., Galvan, C., Neugebauer, M., Lakhina, G. S., Arballo, J. K., et al. (2002). Phase-steepened Alfvén waves, proton perpendicular energization and the creation of magnetic holes and magnetic decreases: The ponderomotive force. *Geophysical Research Letters*, 29(24), 2233. https://doi.org/10.1029/2002GL015652
- Tsurutani, B. T., & Ho, C. M. (1999). A review of discontinuities and Alfvén waves in interplanetary space: Ulysses results. *Reviews of Geophysics*, 37, 517.

BOROVSKY AND BURKHOLDER 17 of 18



- Tu, C.-Y., Wang, X., He, J., Marsch, E., & Wang, L. (2016). Two cases of convecting structure in the slow solar wind turbulence. AIP Conference Proceedings, 1720, 040017.
- Vahala, G., & Montgomery, D. (1971). Kinetic theory of a two-dimensional magnetized plasma. Journal of Plasma Physics, 6, 425.
- Vasquez, B. J., Abramenko, V. I., Haggerty, D. K., & Smith, C. W. (2007). Numerous small magnetic field discontinuities of Bartels rotation 2286 and the potential role of Alfvénic turbulence. *Journal of Geophysical Research*, 112, A11102. https://doi.org/10.1029/2007JA012504
- Vasquez, B. J., & Hollweg, J. V. (2001). Evolution and dissipation of imbedded rotational discontinuities and Alfvén waves in nonuniform plasma and the resulting proton heating. *Journal of Geophysical Research*, 106, 5661.
- Vasquez, B. J., Markovskii, S. A., & Smith, C. W. (2013). Solar wind magnetic field discontinuities and turbulence generated current layers. AIP Conference Proceedings. 1539, 291.
- Verscharen, D., & Marsch, E. (2011). Compressive high-frequency waves riding on an Alfvén/ion-cyclotron wave in a multi-fluid plasma. Journal of Plasma Physics, 77(5), 693–707. https://doi.org/10.1017/S0022377811000080
- Verscharen, D., Marsch, E., Motschmann, U., & Muller, J. (2012). Kinetic cascade beyond magnetohydrodynmics of solar wind turbulence in two-dimensional hybrid simulations. *Physics of Plasmas*, 19(2), 022305. https://doi.org/10.1063/1.3682960
- Wyper, P. F., & Hesse, M. (2015). Quantifying three dimensional reconnection in fragmented current layers. *Physics of Plasmas*, 22(4), 042117. https://doi.org/10.1063/1.4918335
- Xu, F., & Borovsky, J. E. (2015). A new 4-plasma categorization scheme for the solar wind. *Journal of Geophysical Research: Space Physics*, 120, 70–100. https://doi.org/10.1002/2014JA020412
- Yin, L., & Winske, D. (2002). Simulations of current sheet thinning and reconnection. *Journal of Geophysical Research*, 107(A12), 1485. https://doi.org/10.1029/2002JA009507
- Yoshizawa, A., & Yokoi, N. (1996). Stationary large-scale magnetic fields generated by turbulent motion in a spherical region. *Physics of Plasmas*, 3(10), 3604–3613. https://doi.org/10.1063/1.871952
- Zelenyi, L. M., Malova, H. V., Artemyev, A. V., Popov, V. Y., & Petrukovich, A. A. (2011). Thin current sheets in collisionless plasma: Equilibrium structure, plasma instabilities, and particle acceleration. *Plasma Physics Reports*, 37(2), 118–160. https://doi.org/10.1134/S1063780X1102005X
- Zhang, T. L., Russell, C. T., Zambelli, W., Voros, Z., Wang, C., Cao, J. B., et al. (2008). Behavior of current sheets at directional magnetic discontinuities in the solar wind at 0.72 AU. *Geophysical Research Letters*, 35, L24102. https://doi.org/10.1029/2008GL036120
- Zhao, L., Zurbuchen, T. H., & Fisk, L. A. (2009). Global distribution of the solar wind during solar cycle 23: ACE observations. *Geophysical Research Letters*, 36, L14104. https://doi.org/10.1029/2009GL039181
- Zhdankin, V., Boldyrev, S., Mason, J., & Perez, J. C. (2012). Magnetic discontinuities in magnetohydrodynamic turbulence and in the solar wind. *Physical Review Letters*, 108(17), 175004. https://doi.org/10.1103/PhysRevLett.108.175004